Original Article

The International Journal of Robotics Research
2025, Vol. 0(0) 1–23

DOI: 10.1177/02783649251366323
journals.sagepub.com/home/ijr

Model-based control of proprioceptive origami actuators for pneumatic manipulation

Taehwa Hong[1], Jinkyu Yang[1] and Yong-Lae Park[1]

Abstract

This paper introduces a novel approach for designing soft robotic manipulators using origami cylinder modules (OCMs) as building blocks. An OCM is defined as a pneumatically actuated soft robotic unit capable of both linear and bending deformations, contributing to a lightweight and compact robotic system. A rigorous mathematical model was developed to estimate the force and moment outputs of the OCM, with experimental validation confirming the accuracy of the prediction. Multiple OCMs were integrated into a continuum manipulator, and their performance was evaluated by various manipulation tasks. The results demonstrate that the OCM model predicts the behavior of the actuator with a high accuracy in the estimation of force and moment. The origami manipulator also achieves a wide range of motions (ROM) with relatively small errors, showcasing potential for practical applications. These findings introduce a new method for developing soft robotic manipulators made of origami-based air chambers that offer lightweight and compact designs. The mathematical model of the OCM holds implications for simulating actuator behavior in real-world applications, while the performance of the origami manipulator shows the potential for practical implementation. This study provides valuable insights into the advancement of robotic manipulators based on origami structures, allowing a useful set of tools in the field of robotics.

Keywords

origami-inspired robots, origami structure modeling, soft manipulator, proprioceptive actuator

Introduction

Origami-inspired robots have emerged as a novel and versatile category within the field of soft robotics, leveraging the principles of traditional Japanese paper folding to create simple and lightweight structures capable of complex three-dimensional movements (Peraza-Hernandez et al., 2014; Rus and Tolley 2018; Turner et al., 2016). This innovative approach has found applications across diverse sectors, including manufacturing (Meloni et al., 2021), biomedical devices (Johnson et al., 2017), and space exploration (Nishiyama 2012), where the unique properties of origami robots, such as the ability to fold flat, a wide range of motion (ROM), a considerable amount of force, are particularly beneficial. The inherent compliance and adaptability of origami-utilized soft robots also make them ideal for safe interaction with humans and delicate surroundings (Laschi et al., 2016).

Despite these advantages, the control of origami robots poses significant challenges due to the complexities involved in accurate modeling of their kinematics and dynamics (Kim et al., 2021; Wang et al., 2018). The nonlinear nature of folding mechanisms (Tachi 2010), coupled with variations in material properties (Ji et al., 2021), complicates the prediction and control of these systems. Researchers have attempted to overcome these hurdles through various model-based control strategies, including finite element analysis (FEA) (Grazioso et al., 2019), lumped parameter models (Della Santina et al., 2020), and machine learning techniques (Thuruthel et al., 2018).

[1]Department of Mechanical Engineering; Institute of Advanced Machines and Design; Institute of Engineering Research, Seoul National University, Seoul, Republic of Korea

Corresponding authors:
Jinkyu Yang, Department of Mechanical Engineering, Seoul National University 1 Gwanak-ro, Gwanak-gu, Seoul 08826, Korea.
Email: jkyang11@snu.ac.kr

Yong-Lae Park, Department of Mechanical Engineering, Seoul National University 1 Gwanak-ro, Gwanak-gu, Seoul 08826, Korea.
Email: ylpark@snu.ac.kr

Furthermore, geometric and strain energy-based modeling approaches have been widely employed to describe origami structures (Kaufmann et al., 2022; Zhang et al., 2021). These methods have been particularly effective in capturing the deformation characteristics of Yoshimura-patterned actuators, as seen in prior studies employing internal balloon actuators or hybrid actuation mechanisms (Zhang et al., 2024). However, these approaches often assume simplified mechanical approximations that limit their applicability to real-time control. Moreover, inverse kinematics (IK) solutions in origami-inspired manipulators are typically formulated either through rigid-link approximations (Zhang et al., 2024) or iterative numerical optimization (Santoso and Onal 2021), which increase the computational complexity.

To address the issues in heavy computation and real-time state estimation in the soft manipulator, researchers have explored the use of proprioceptive soft actuators capable of detecting their own internal states, such as current positions, bending angles, or even forces, without the need to add external sensors. Specifically in soft robots, the systems are designed to detect the deformation or motion states of the actuators directly, providing an alternative to relying solely on modeling (Li et al., 2022; Luo et al., 2017; Wang and Chortos 2022). These types of proprioceptive soft actuators have self-sensing mechanisms, which typically employ resistive (Ku et al., 2024; Truby et al., 2020; Wirekoh et al., 2019; Zhou et al., 2020) and capacitive (Dawood et al., 2020; Scimeca et al., 2019) sensors or optical (Choi et al., 2023; Jung et al., 2020; Kang et al., 2023) sensors to measure the strain, orientation or bending curvature of the soft manipulators. Although this self-sensing capability offers unique advantages, fabrication can be challenging due to the process of integrating complex components into the mechanisms or structures. Accurate measurement of the configuration of a proprioceptive soft manipulator often requires multiple sensors, leading to difficulties in fabrication and calibration. These requirements result in a system that is not only bulky, but also complex due to the need for a wide sensing range and robustness against noise (Laschi et al., 2016; Thuruthel et al., 2019).

In this paper, our aim is to tackle the dual challenges of computational complexity in model-based control methods and the difficulties in precise estimation of the configuration of soft origami manipulators. Our approach encompasses the development of a highly functional soft manipulator utilizing solely origami structures, coupled with the derivation of a simplified kinematic model. To begin with the development of the soft manipulator, we first propose the design of modularized, pneumatically driven bellow-type actuators by incorporating an origami cylinder structure into the architecture of soft manipulators with an embedded self-sensing mechanism at each module. The use of cylindrical origami patterns, such as the Yoshimura or Kresling design, brings about two principal benefits: the intrinsic functionality of the origami structure itself and a significant simplification in the kinematics of motion (Vander Hoff et al., 2014; Zhang et al., 2023). The origami cylinders are characterized by their elastic properties, which enable axial collapse along predefined folding lines, akin to a spring mechanism (Filipov et al., 2015; Hong et al., 2020; Westra et al., 2021). This feature allows for broad, compliant movements that are ideally suited to the demands of soft actuators used in different robotic systems, such as gripper (Chen et al., 2021; Li et al., 2019), manipulators (Santoso and Onal 2021; Suzuki and Wood 2020), and locomotive robots (Sivaperuman Kalairaj et al., 2021; Yu et al., 2020). Furthermore, when it comes to pneumatically powered, origami cylinders provide a large ROM, force, and ease of reconfiguration, increasing their versatility and effectiveness in various soft robotic applications (Lee and Rodrigue 2019; Zaghloul and Bone 2023; Zou et al., 2021). However, in spite of the uniqueness and the strength of the origami cylinder, there are few applicable methods practically available to estimate the kinematics, especially when actuated pneumatically. Instead, a great deal of research is known to analyze the origami cylinder in static manner. Conventionally, complex origami structures have been analyzed using non-linear FEA (Liu and Paulino 2017), post-buckling analysis (Hunt and Ario 2005), and numerical simulations (Liu and Paulino 2016; Zhu et al., 2022), estimating the deformation of thin-walled rigid structures similar to those of origami. Although the solving methods are well defined, they are still complex and computationally expensive to use in dynamic scenarios.

Therefore, we propose a simplified kinematic model for our soft manipulator. The main idea of the simplified kinematic model is to bring in the essential assumptions and features from the prior works and simplify the structure (Filipov et al., 2015; Russo et al., 2023; Zhang et al., 2021). The proposed model establishes a mapping of three important parameters: the 3D configuration of the origami actuator, the input signals, and the applied external loads. This allows us to reduce the complexity of the required sensor system to a single length-sensing unit that is compact and does not interfere with the process of estimating the kinematics and controlling the manipulator. By integrating the proposed simplified model with proprioceptive characteristics, this approach effectively controls the soft manipulator. It takes advantage of both model-based and proprioceptive methods in a synergistic way.

In summary, this study presents three main contributions. First, a modularized pneumatic actuator is designed and fabricated using the Yoshimura origami cylinder, which features proprioceptive functions to measure its configuration. These modules are integrated into an extended soft manipulator system, showing promise for diverse applications. Secondly, a simplified kinematic model for the origami cylinder is proposed, enabling accurate pose estimation in conjunction with its self-sensing mechanisms. The derived model uses a minimal proprioceptive sensing

mechanism, significantly simplifying the control strategy while maintaining high performance and reliability. Finally, a continuum robot made of multiple actuation units called origami cylinder modules (OCMs) has been demonstrated in various applications, such as object picking and manipulation using an integrated gripper and performing path-planning tasks. These applications demonstrate the versatility of the developed OCMs, highlighting their potential in practical use cases, such as precise object handling, trajectory following, and modular extension of robotic systems.

Materials

This section describes the proposed design of a soft manipulator that utilizes pneumatically actuated origami actuators, as depicted in Figure 1(A). The manipulator was constructed using multiple OCMs, each of which shows the characteristic properties of the Yoshimura cylinder, enabling both linear and bending deformation. Figure 1(B) briefly illustrates the OCM fabrication process using polyethylene terephthalate (PET) films and polypropylene (PP) sealing tapes. More details on the fabrication and the material selection criteria are described in Supplemental Information–A.

Figure 1(C) shows the design of the OCM and its sensing mechanism. For detecting longitudinal displacement, a hall effect sensor (SS41, Honeywell) and a neodymium magnet were installed in the hollow air chamber of the cylinder. This sensor module was compact and did not interfere with the existing structure, providing a linear response to the distance between the sensor and the magnet (see Supplemental Information–B). Each OCM actively contracts and extends in the range of −60% to 60% of its initial length of 40 mm and to bend up to 1.5 radians. The single OCM is as light as approximately 25 g, primarily due to its base material, thin PET films. Most of the weights are attributable to the 3D printed parts.

The continuum robot is composed of extended OCMs arranged in parallel, as shown in Figure 1(A). To facilitate a more straightforward kinematic analysis, the design commonly adopts a piecewise constant curvature (PCC) approach for the continuum robot, as suggested in previous

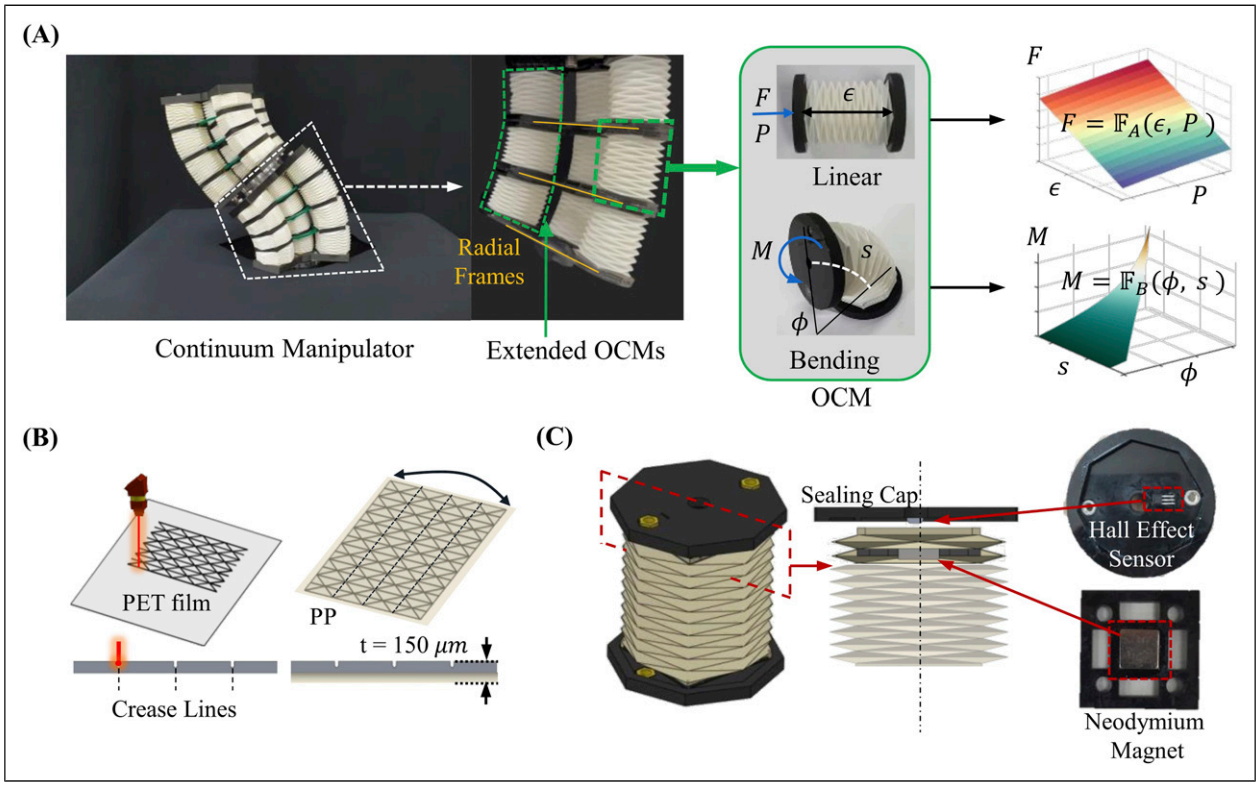

Figure 1. (A) Proposed origami continuum manipulator, comprising two segments. Each segment was constructed from multiple OCMs, of which is capable of generating both linear and bending motions. The characteristics of these two distinct deformation modes are analyzed. (B) Fabrication of a pneumatic chamber based on the Yoshimura cylinder pattern. This pattern was engraved on a 100 μm polyethylene terephthalate (PET) film using the laser CNC machine (Trotec Speedy 300, Trotec) and sealed with 50 μm polypropylene (PP) tape to create an airtight chamber. The cylindrical shape was formed, and then the Yoshimura origami pattern was folded. (C) 3D-printed air sealing caps and neodymium magnet located inside the folded Yoshimura pattern. A hall-effect sensor and a neodymium magnet were used to measure the displacement of a single layer of the actuator.

studies Webster III and Jones (2010), Grazioso et al. (2019). In this configuration, the OCMs were connected using a radial frame, shown in Figure 1(A)) to establish a uniform curvature across each single segment of the robot. There are four extended OCMs in the design, three were strategically positioned in an equilateral, which was essential for generating the actuation motions of the module. The fourth cylinder, located at the centroid of the triangle, plays a role as a structural backbone, adding an additional stiffness (Al Abeach et al., 2017) to the manipulator and covering the connecting components, such as electric wires and pneumatic tubes.

Model

The proposed OCM comprises a cylindrical chamber crafted using the Yoshimura pattern. The Yoshimura cylinder is generally known to be a volumetric origami structure that is rigid when folded properly (Suh et al., 2022). However, it exhibits the ability to deform under specific conditions when constructed from materials with low stiffness (Martinez et al., 2012; Zhang et al., 2020). The deformation of the cylinder along the crease lines and the thin facets occurs due to axial compression, extension, and bending (Cai et al., 2016). Moreover, the Yoshimura cylinder has considerable torsional stiffness, which allows the twisting motion to be neglected in the analysis (Santoso and Onal 2021).

The objective of modeling is to analyze the kinematics of the Yoshimura cylinder on the basis of its volumetric origami characteristics. Given its linear volume reduction, its axial strain (ϵ) can be defined as the ratio of the change in axial length ($l - l_0$) to the original length (l_0):

$$\epsilon = \frac{l - l_0}{l_0}. \tag{1}$$

The initial length (l_0) is the design parameter determined when the pattern is made. The Yoshimura cylinder can also be bent, resulting in the bending angle (ϕ), the curvature (κ), and the length of the neutral axis for bending (s). Thus, the configuration ($\mathcal{C}$) of the actuator includes these variables alongside the axial strain (ϵ), as shown in Figure 1(A). The controllable inputs of the system are the pressure of the compressed air (P) and the external load (τ), and τ accounts for both force (F) and moment (M). The aim is to derive the relationship between the input and the output elements expressed as f_y, which will be the kinematic function:

$$\tau_{ext} = f_{OCM}(P, \mathcal{C}), \tag{2}$$

where $\mathcal{C}$ represents the geometric information of the Yoshimura cylinder that determines the configuration, as shown in Figure 2(A).

Design parameters of the Yoshimura cylinder

The kinematic behavior of the Yoshimura cylinder, shown in Figure 2(A) with its characteristic repeated patterns, is affected by several design parameters. We identify the smallest foldable unit within these patterns as a single layer, constructed by tessellating identical isosceles triangles. For the OCM design, it is assumed that all N layers are repeated and experience uniform deformations. Therefore, this single layer plays a crucial role in determining both the ROM and the overall configuration of the actuator. Each single layer consists of an isosceles triangle that has two parameters: the length of the base side (L) and the angle of the side (θ_d), as depicted in Figure 2(A). Table 1 summarizes the design parameters considered in the analysis.

Assumptions for pattern analysis on Yoshimura origami cylinder

Three assumptions were adopted to simplify the actuator characterization. First, the actuator is considered as a conservative system, allowing the application of the virtual work principle to correlate the external force with the configuration of the actuator (Chou and Hannaford 1996). This approach facilitates a straightforward relationship between the applied forces and the resulting deformations. Second, we assume an uniform stress distribution across the entire cylindrical structure, leading to consistent deformation across all layers, whether through linear compression/extension or bending. Given that the cylinder comprises repeated single layers, the entire structure can be conceptualized as a stack of multiple layers, as shown in Figure 2(A). Consequently, the kinematics of this single layer is uniformly applicable to the entire structure. Lastly, for analytical simplicity, the cylinder is simplified as a truss structure, serving as a simplified equivalent model. As illustrated in Figure 2(C), a single layer forms a polyhedron consisting of 16 isosceles triangles, creating a closed structure with 12 vertices and 40 edges. Figure 2(B) depicts the abstraction of the Yoshimura cylinder model, where the vertices and edges are represented as nodes and elastic bar elements, respectively, with each edge modeled as an elastic bar with a single degree of freedom (DOF) that can store strain energy through deformation. Also, rotational springs simulate the hinges of the origami to capture the elastic deformations along the crease lines. The potential was calculated based on the amount of rotation angle between the neighboring facets that share each hinge (Kshad et al., 2018). Moreover, due to the non-linear deformation experienced by the Yoshimura cylinder as a result of its rigidity, previous studies dealing with volumetric origami structures have incorporated additional elements to account for the facet deformation of the origami structure (Filipov et al., 2015; Liu and Paulino 2016; Zhang et al., 2021). Referring

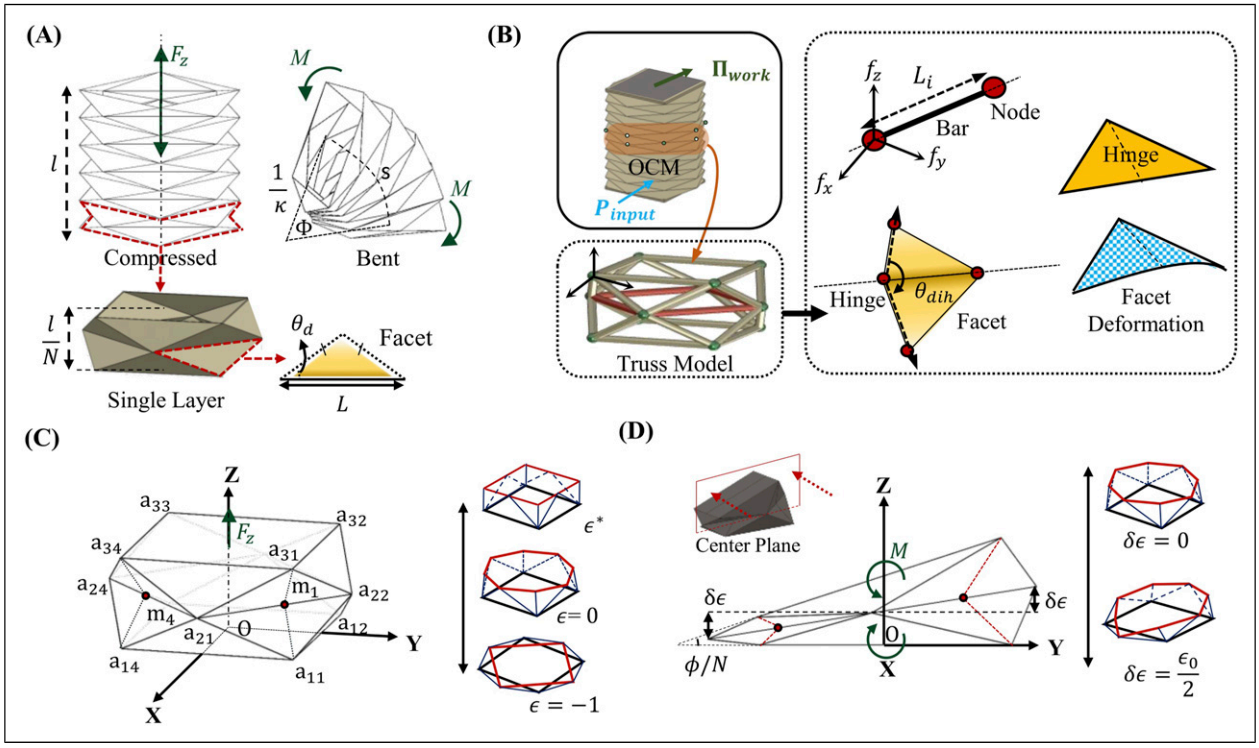

Figure 2. (A) Configuration of the Yoshimura origami cylinder and the definition of a single-layer. (B) Yoshimura origami cylinder treated as energy-conserving, with each vertex represented as a node and each edge as an elastic bar element with a single DOF. Rotational springs simulate hinge deformations, accounting for the nonlinear facet behavior. (C) Nodes indication of the single layer and linear deformation when axial force (F_z) applied (left) and the brief deformation configuration according to the strain ϵ (right). By the definition, ϵ can vary from -1 to the bounded maximum value ϵ^* that is the geometric limit. (D) Bending configuration of the single layer when moment M is applied and with bending angle ϕ/N. The bending angle can be expressed with the parameter $\delta\epsilon$ and has a range from 0 to $\epsilon_0/2$.

to these results, we also adopted some basic features in the simplified model, as shown in Figure 2(C). The figure details the arrangement of 12 nodes ($a_{11} \sim a_{34}$) and an additional four nodes ($m_1 \sim m_4$) added at the midpoint of the horizontal edges to simulate the facet deformation. The truss model employs the properties of virtual materials, with two defined stiffness coefficients (k_b and k_h) representing the axial and torsional resistance, respectively, to accurately reflect the kinematics of the actual structure. From the first assumption that the actuator behaves as a conservative system, the total potential energy stored in the origami cylinder can be expressed as:

$$\Pi_{total} = \Pi_{bar} + \Pi_{hinge} - \Pi_{work}, \tag{3}$$

where each term represents a different contribution to the system's energy:

- Π_{bar}: The strain energy of the bar elements accounts for the elastic deformation along the edges of the origami structure. This strain energy is calculated based on the elongation or compression of the bar elements, which is directly related to the nodal displacement and the geometric configuration of the Yoshimura cylinder.
- Π_{hinge}: The rotational energy stored in the crease lines reflects the energy required to rotate the facets relative to each other. This is determined by the change in the dihedral angles between the adjacent facets, computed from the nodal positions and the geometric constraints of the pattern.

Table 1. Design parameters and specifications.

Design parameters	L	30 mm
	l_0	40 mm
	θ_d	π/8 rad
	N	10
	n_b	40
	n_h	32
	w	13 g
Fitting coefficients	k_b	1.3 N/m
	k_h	0.1 N/m
Manipulator	w_M	238 g
	d	60 mm
	s_c	210 mm

- Π_{work}: The work done by the applied pressure, accounting for the external force applied to the structure. The work is calculated as the product of applied pressure and the change in volume as the cylinder deforms.

The calculation of the total potential energy also incorporates the principle of virtual work during deformation, which accounts for changes in the relative positions of the nodes and the dihedral angles between facet pairs.

Given our assumption of uniform deformation across the structure, the analysis of potential energy focuses on determining the nodal displacements within a single layer. The geometric constraints inherent in the Yoshimura pattern were used to calculate the position and deformation of each node by solving a system of multi-variable equations.

In order to clarify further, the first segment of the kinematic derivation focuses on the axial deformation of the Yoshimura cylinder, which is a purely linear deformation. This type of deformation is depicted in Figure 2(A). The second segment of the kinematic derivation focuses on bending deformation, which can occur simultaneously with axial deformation in the Yoshimura structure. To ensure a comprehensive analysis, these types of motion are treated in separate analytical processes, allowing a detailed examination of each type of deformation.

Kinematics modeling of the Yoshimura cylinder

Axial kinematics. The axial deformation kinematics of a single layer in the Yoshimura cylinder is determined by correlating the axial force (F_z) with the input pressure (P) and the strain (ϵ), as represented as

$$F_z = \mathbb{F}_A(\epsilon, P). \tag{4}$$

Here, $\mathbb{F}_A$ is a function shown in Figure 1(A), derived from three potential energy components outlined in equation (3). The potential energy within the bar elements (Π^A_{bar}) is expressed as

$$\Pi^A_{bar}(\epsilon) = N \sum_{i=1}^{n_b} \frac{1}{2} k_b (L_i(\epsilon) - L_i(\epsilon_0))^2, \tag{5}$$

where ϵ_0 represents the initial strain when the cylinder is unloaded and at a neutral state. These type of strain energy based analysis is well defined method as shown in prior works (Zhang et al., 2021) in Yoshimura origami structure. Due to the geometric constraints of the Yoshimura cylinder, the parameter ϵ is bounded theoretically in $\epsilon \in [-1, \epsilon^*]$, where ϵ^* is the value of $L \tan \theta_d$, the height of the isosceles triangle (see Figure 2(A)). In Figure 2(C), there are a total of n_b bar members shown in a three-dimensional coordinate system. The length of i^{th} member is a function of ϵ and expressed as $L_i(\epsilon)$. Assuming the uniform load distribution across each i^{th} member, the potential energy is calculated with a constant stiffness per unit length k_b, and the length of each bar element at a certain strain (ϵ) can be calculated based on the distance between each node and the geometric constraints of the Yoshimura cylinder. The detailed coordinates of the nodes and the geometric constraints were described in Supplemental Information–C.1.

The subsequent terms corresponds to the potential energy of the rotational hinges due to the angle variation between the facets, which can be expressed as

$$\Pi^A_{hinge}(\epsilon) = N \sum_{i=1}^{n_h} \frac{1}{2} k_h L_i(\epsilon) |\theta_i(\epsilon) - \theta_i(\epsilon_0)|^2. \tag{6}$$

A dihedral angle (θ_{dih}) is defined as the angle between two adjacent facets in a single layer, as shown in Figure 2(B). In a single layer, there are a total of n_h dihedral angles that can be defined by combinations of two neighboring facets connected to each hinge. Similarly to equation (5), the strain energy resulting from the angle change was considered in the folding lines. The coefficient representing the rotational stiffness per unit length is denoted by k_h which is multiplied by all the lengths of the hinge members $L_i(\epsilon)$ when calculating the total potential energy. The types of dihedral angles in an axial deformation case are summarized in Supplemental Information–C.1.

The final component considers the volume change due to the applied pressure (P) inside the actuator. The volume of a single layer under strain ϵ is set to $V_A(\epsilon)$ and can be easily calculated using the nodal positions. Hence, the virtual work resulting from the pressure P can be explicitly derived as

$$\Pi^A_{work}(\epsilon, P) = P \Delta V_A = P(V_A(\epsilon) - V_A(\epsilon_0)), \tag{7}$$

which is linearly proportional to pressure P.

Eventually, the three terms that comprise equation (3) can be expressed using the design parameters (N, θ_d, L, and l_0) and two fitting parameters (k_b and k_h). Incorporating equations (5)–(7) into equation (3) allows the total potential to be articulated as a function of strain (ϵ) and pressure (P) as the following:

$$\Pi^A(\epsilon, P) = \Pi^A_{bar}(\epsilon) + \Pi^A_{hinge}(\epsilon) - \Pi^A_{work}(\epsilon, P). \tag{8}$$

The axial force is equal to the derivative of the axial potential energy, with the variable ϵ under an assumption of energy conservation. Therefore, the kinematics related to the net axial force (F_z) and the strain (ϵ) can be expressed as

$$F_z(\epsilon, P) = \frac{\partial \Pi^A(\epsilon, P)}{\partial \epsilon} := \mathbb{F}_A(\epsilon, P) \tag{9}$$

maintaining the form presented in equation (4).

Bending kinematics. When subjected to a load that induces a moment, the Yoshimura cylinder undergoes bending

deformation. The bending deformation of the single layer is characterized by two configuration variables, the neutral axis length (s/N) and the bending angle (ϕ/N) of the cylinder. Let us define a function $\mathbb{F}_B$ that correlates the moment in a single layer with configuration variables as

$$M = \mathbb{F}_B(\phi/N, s/N). \tag{10}$$

Assuming identical deformations across all N layers, a moment M applied to the entire cylinder affects each layer uniformly, and the bending angle is also divided equally with the number of layers as ϕ/N. Due to the structural symmetry of the cylinder, each layer exhibits a pure bending deformation. Figure 2(D) illustrates the deformation of a bent single layer from the perspective of the y-z center plane, where the displacement of the node corresponds to the bending angle ϕ/N. For example, the nodes a_{22} and a_{24}, initially at the same coordinate on the z-axis ($1/2l_0N$), indicating the initial axial strain, move symmetrically. These coordinates will move in the opposite direction but with the same magnitude. If this magnitude of z-coordinate deviation defined as δl, z-coordinates of the nodes a_{22} and a_{24} will eventually move to ($1/2l_0N + \delta l$) and ($1/2l_0N - \delta l$), respectively. The variable δl was used for the simple expression of all node positions, which depends on the bending angle ϕ/N and the length of the neutral axis s/N. The geometric relationship between the original configuration (ϕ, s) and δl can be derived and depicted in Figure 3(A), introducing additional angles and edge lengths for calculation. Two angles defined in the y-z plane as

$$\begin{aligned} \theta_1(\delta l, l_0) &= \sin^{-1}\left(\frac{l_0/2N - \delta l}{L\tan\theta_d}\right), \text{ and} \\ \theta_2(\delta l, l_0) &= \sin^{-1}\left(\frac{l_0/2N + \delta l}{L\tan\theta_d}\right). \end{aligned} \tag{11}$$

These two angles can be expressed with variables δl and l_0. By using these angles, the additional edge lengths defined as $t_1 \sim t_3$ can be expressed as

$$\begin{aligned} t_1(\delta l, l_0) &= L\tan\theta_d\cos\theta_1, \\ t_2(\delta l, l_0) &= L\tan\theta_d\cos\theta_2, \text{ and} \\ t_3(\delta l, l_0) &= \frac{L\tan\theta_d\sin\theta_1}{\tan(\phi/2N)}. \end{aligned} \tag{12}$$

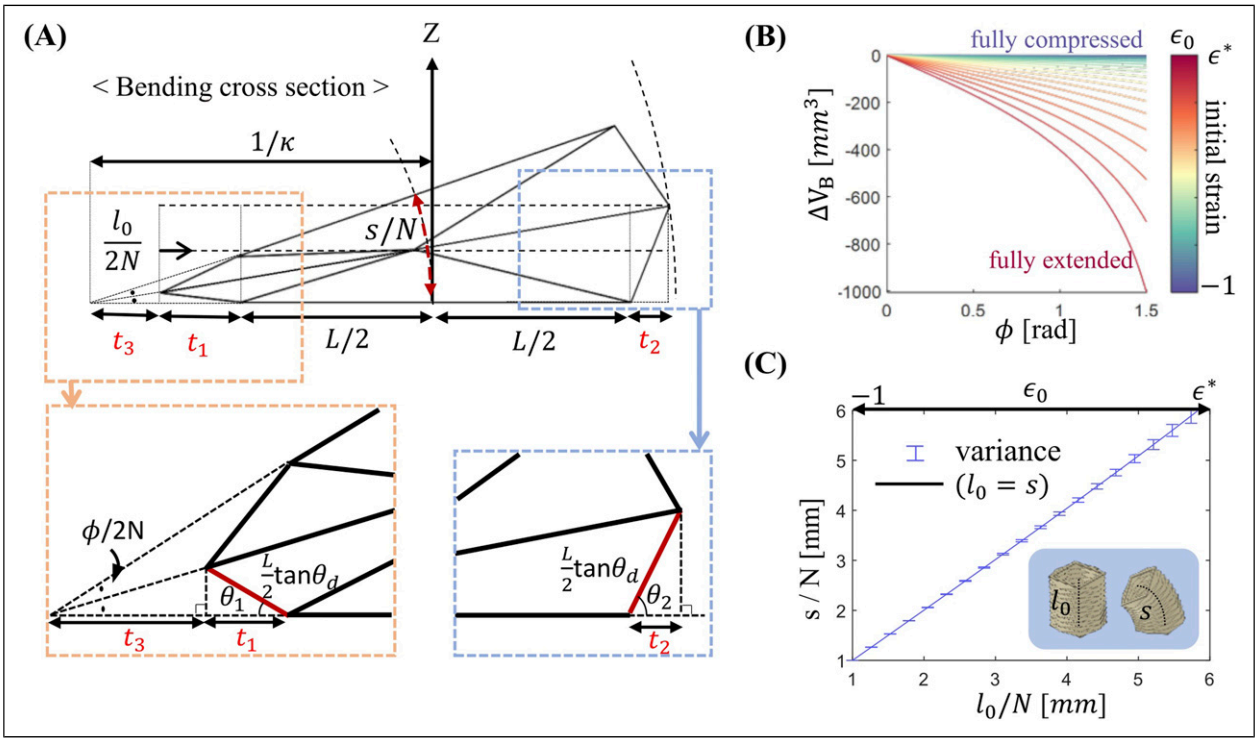

Figure 3. (A) Cross section of a single layer under pure bending. Additional variables (t_1, t_2, and t_3) are defined and depicted in the cross section of the single layer. These variables are used to derive the relation between the configuration parameters (ϕ, κ, and s) with the length l. (B) Numerical volume variation by the bending angle (ϕ/N) calculated for each initial strain (ϵ_0) from -1 to ϵ^*, as shown with the color code. The larger initial strain gives the larger variation. (C) Backbone length (s) of the single layer maintained the same as the initial value l_0, during bending. The solid line shows the numerical calculation of s compared with the initial length l_0/N of the single layer. The maximum deviance was 0.183 mm at l_0/N = 6 mm, where the strain was the maximum ϵ^*.

These variables allow the derivation of the bending angle and the curvature of the N-layered cylinder as

$$\phi(\delta l, l_0) = 2N \tan^{-1}\left(\frac{L\tan\theta_d \sin\theta_1}{t_3}\right), \tag{13}$$

$$R(\delta l, l_0) = t_1 + t_3 + L/2, \text{ and } \kappa(\delta l, l_0) = \frac{1}{R}. \tag{14}$$

Since the curvature is uniform across the single layer, the length of the neutral axis s (or the backbone length) can be considered as an arc length, which is

$$s(\delta l, l_0) = R\phi. \tag{15}$$

Based on equations (13)–(15), the functions related to the configuration parameters of the single layer were all related to the variables δl and l_0. The range of the feasible bending angle is also determined by the constraints condition from the initial length (l_0) of the single layer. For example, in a single layer, the value of the z-axis of the node a_{24} cannot be negative due to the geometric constraints imposed by the neighboring layer. Therefore, the feasible range of δl is $0 < \delta l < l_0/2N$.

A notable result here is that l_0 or s is independent of the bending angle ϕ/N. This characteristic is verified numerically by calculating the positions of all nodes and actually confirming the equation (15). As plotted in Figure 3(C), once the initial height l_0/N of the single layer is set by the axial deformation from equation (24), s remains constant to the backbone length before the bending deformation with the maximum numerical error 0.183 mm. This indicates that bending can be decoupled from axial deformation from equation (24), with pressure and axial force affecting only the longitudinal length (l_0) or the neutral axis length (s).

The potential energy in the virtual bar and the hinge elements can be obtained based on the coordinates expressed in terms of δl, applying the same geometric constraints as in the axial kinematics (see Supplemental Information–C.2). Once node displacement is determined, the facets deform, altering dihedral angles. The potential energy in the bar (Π^B_{bar}) and the hinge elements (Π^B_{hinge}), together with the work done by the pressure (Π^B_{work}), can be formulated as

$$\Pi^B_{bar}(\delta l, l_0) = N\sum_{i=1}^{n_b}\frac{1}{2}k_b(L_i(\delta l + l_0) - L_i(l_0))^2, \tag{16}$$

$$\Pi^B_{hinge}(\delta l, l_0) = N\sum_{i=1}^{n_h}\frac{1}{2}k_h L_i(\delta l)|\theta_i(\delta l + l_0) - \theta_i(l_0)|^2, \text{ and} \tag{17}$$

$$\Pi^B_{work}(\delta l, l_0) = P\Delta V_B(\delta l, l_0). \tag{18}$$

Similar to the axial deformation case, there are various combinations of facet pairs and corresponding dihedral angles (see Supplemental Information–C.2). Here, ΔV_B denotes the bending-induced volume change. The volume of the single layer can be calculated in a numerical way using tetrahedral decomposition based on the positions of the nodes (Ho-Le 1988). Figure 3(B) displays the curves if ΔV_B is a function of the bending angle (ϕ/N) at each initial strain (ϵ_0). Since the feasible range of the (ϕ/N) becomes larger as the length (l_0/N) (or the initial strain (ϵ_0)) before the bending increases, allowing for more significant volume deviations. Unlike the axial case, where the volume change (ΔV_A) could be explicitly formulated, the volume change in the bending scenario is determined through numerical calculation and the results are plotted in Figure 3(C).

Eventually, the total potential energy stored in a single layer by the bending moment is given by

$$\Pi^B(\delta\epsilon, \epsilon_0) = \Pi^B_{bar} + \Pi^B_{hinge} - \Pi^B_{work}. \tag{19}$$

Here, δl and l_0 are changed to strain $\delta\epsilon$ and ϵ_0, respectively, using equation (1) to align with the axial kinematics for consistent notation. The bending moment of the actuator is derived by differentiating equation (19) with respect to the bending angle (ϕ) from equation (13) which is

$$\widetilde{M}(\delta\epsilon, \epsilon_0) = \frac{\partial\Pi^B(\delta\epsilon, \epsilon_0)}{\partial\phi(\delta\epsilon, \epsilon_0)}. \tag{20}$$

The moment derived from the derivative of the potential energy is expressed with the substitute variable $\widetilde{M}$ in equation (20). This is because the original target kinematics equation was in the form of equation (10), which directly relates the configuration ϕ and s to the moment. Instead, since all configuration parameters are functions of $\delta\epsilon$ and ϵ_0, it is possible to define the same moment function but in a different form that reflects this dependency as

$$M(\phi, s) = \widetilde{M}(\delta\epsilon, \epsilon_0), \text{ and } \mathbb{F}_B(\phi, s) := M(\phi, s), \tag{21}$$

aligning with the original formulation in equation (10).

Integrated kinematics. Leveraging the geometric constraints and the structural assumptions outlined earlier, the kinematics of the linear and bending deformations have been decoupled into two different types of configuration change. The axial height (l_0) or the initial strain (ϵ_0) was solely determined by the axially applied force denoted by F_z and the pressure input P. Once this axial configuration is established, an applied moment (M) induces bending in the cylinder, altering configuration variables, such as the bending angle (ϕ) and the backbone length (s). When an external force $\overrightarrow{f_{ext}} = [F_x, F_y, F_z]^T$ is applied to the tip of the Yoshimura cylinder, the axial component force F_z, influences the axial elongation, while the lateral components (F_x

and F_y) contribute to the generation of a moment. The resultant moment is only the direction causing the cylinder to bend (M in equation (21)), given that twisting moments are considered negligible and the bending orientation is nonspecific due to the symmetrical shape of the cylinder. Consequently, the external load can be represented as

$$\tau_{ext} := \begin{bmatrix} F_z \\ M \end{bmatrix}. \tag{22}$$

Given that both components of the τ_{ext} were already derived in equations (9) and 21, the kinematics can be integrated into

$$\tau_{ext} = \begin{bmatrix} \mathbb{F}_A(\epsilon, P) \\ \mathbb{F}_B(\phi, s) \end{bmatrix} = f_{OCM}(P, \mathcal{C}), \tag{23}$$

which is a comprehensive formulation in a form of the target kinematics model equation (2). Therefore, the configuration parameter $\mathcal{C}$ effectively encapsulates ϵ, ϕ, and s, offering a unified approach to describe the kinematics of the Yoshimura cylinder.

Inverse mapping using lookup table methods

To efficiently compute the forward and inverse kinematics (FK/IK) of the origami manipulator for real-time control tasks, a data-driven approach using lookup tables (LUTs) was employed. Based on the FK mapping function in equation (23), an inverse mapping function was derived to estimate the actuator deformation when the input and the external loads are given. The inverse kinematics of the OCM can be formulated using two inverse functions: $\mathbb{F}_A^*$, which maps the axial force to strain (ϵ) and $\mathbb{F}_B^*$, which maps the bending moment to configuration $\mathcal{C}$. These mappings are not analytically tractable due to the complex interaction between structural elasticity and pneumatic actuation. Instead, a dataset is precomputed through high-fidelity simulations (Supplemental Video 1, Supplemental Information–E), creating a structured LUT for rapid inference.

For each OCM, a dataset of (F_z, P, ϵ) values is generated over fine intervals, allowing efficient interpolation:

$$\epsilon = \mathbb{F}_{\mathbb{A}}^{\dagger}(F_z, P). \tag{24}$$

Similarly, for bending estimation, the precomputed values for bending angles ϕ are stored as:

$$\phi = \mathbb{F}_{\mathbb{B}}^{\dagger}(M, s). \tag{25}$$

Using these inverse mapping functions, given a known external force and pressure, we directly retrieve or interpolate the corresponding strain and bending parameters. Furthermore, these functions allowed to simplify the kinematic modeling of the manipulator and conduct the model-based control in real time. The detailed structure of the LUT used in the controller and the searching algorithms are explained in Supplemental Information–H.

Model of the origami manipulator

The kinematic model of the Yoshimura cylinder, as derived in the previous sections, establishes a foundational relationship between the OCMs and the soft continuum manipulator made of the OCMs. Although the forward kinematics (FK) and the inverse kinematics (IK) for continuum robots, similar to our origami manipulator, are well developed (Jones and Walker 2006; Ku et al., 2024). These models require the prior knowledge of the mapping function that relates the length of the actuator and the input signals. Tendon-driven actuators often estimate their lengths using the measurements from multiple encoders, but pneumatic actuators lack the capability of directly measuring the length information without employing additional modeling or sensors. Thus, the derived kinematic modeling (equation (23)) becomes essential for estimating the state of the continuum manipulator.

Our continuum robot features multiple segments or trunks, each powered by three independently operated actuators, similar to ours shown in Figure 4(A). The FK model of such manipulators involves mapping of each length of the actuator ($l_1 \sim l_3$) to the configuration of the manipulator (Jones and Walker 2006; Ku et al., 2024). As shown in Figure 4(B), there are three parameters required to minimally determine the configuration of a single trunk, the length of the backbone (S_c), the bending angle of the trunk (θ_c), and the bending axis direction angle (ϕ_c), which are calculated as

$$\begin{aligned} S_c &= \frac{1}{3}(l_1 + l_2 + l_3), \\ \theta_c &= \frac{2\sqrt{l_1^2 + l_2^2 + l_3^2 - l_1 l_2 - l_2 l_3 - l_1 l_3}}{3d}, \text{ and} \\ \phi_c &= \tan^{-1}\left(\frac{l_3 + l_2 - 2l_1}{\sqrt{3}\,(l_2 - l_3)}\right). \end{aligned} \tag{26}$$

Assuming the PCC condition for each segment, where no buckling and twist occur in each trunk, and having a unique curvature, the position and the orientation of the tip at the moving platform can be uniquely determined (Grazioso et al., 2019). This results in the special Euclidean group SE (3) transformation from the base frame $\{B\}$ to the moving frame $\{S\}$ being calculable using the configuration parameters detailed in equation (26) above (see Figure 4(C)).

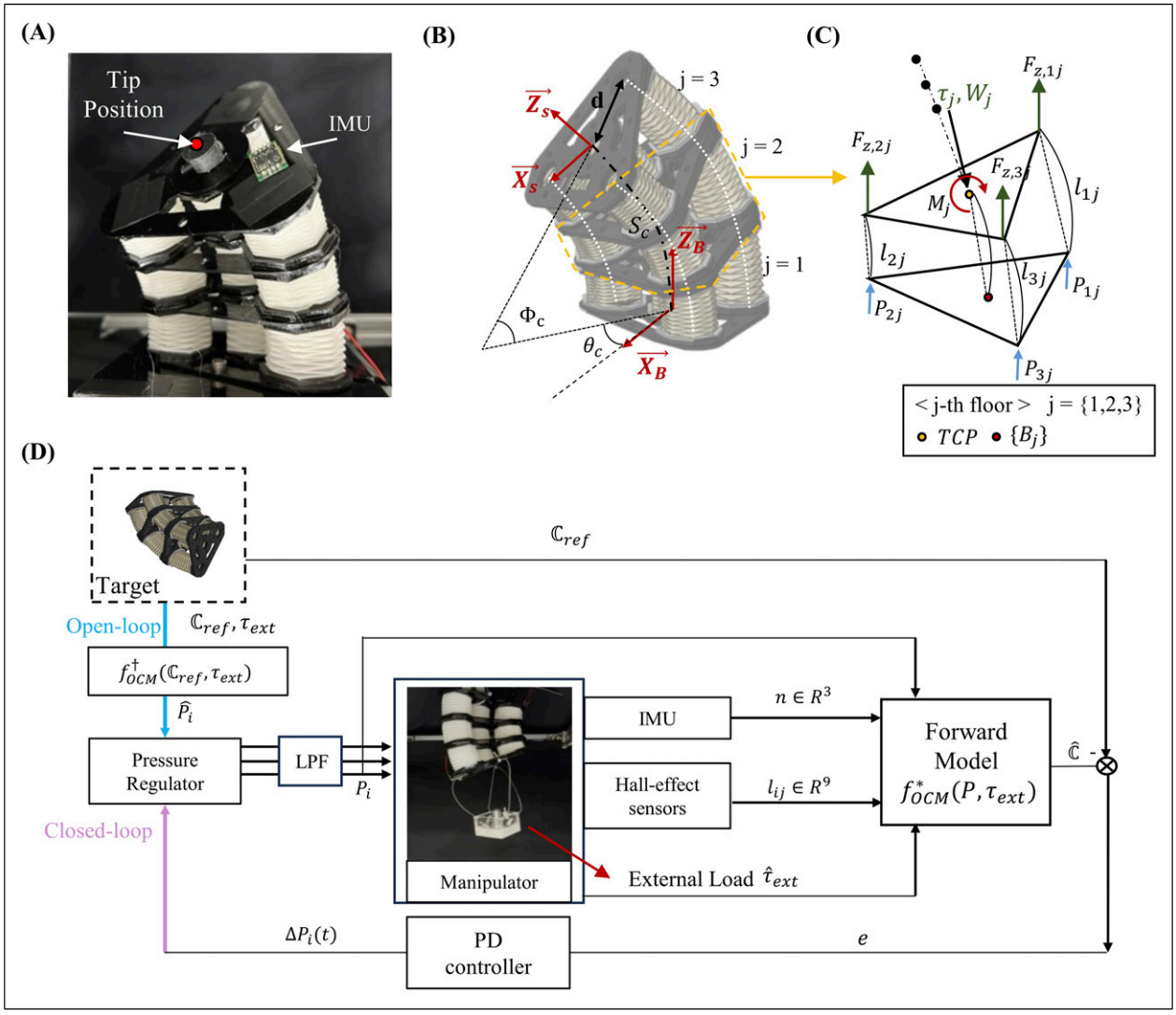

Figure 4. (A) Continuum origami manipulator with OCMs. (B) Configuration information of the origami manipulator, showing two different frames: the fixed base coordinate B_j and the moving frame S_j for each j^{th} parallel manipulator segment. The introduced manipulator in this paper has three segments, indicated by dashed lines. (C) Simplified drawing the j^{th} segment, with three pressure inputs (P_1 to P_3) independently controlling the three actuators. The mass load from neighboring segments (W_j) and the external loads (τ_j) are accounted for in the kinematics. The actuator lengths (l_{ij}) can be estimated using the derived inverse mapping functions. (D) Control schematic of the origami manipulator. The closed-loop system controls the manipulator to reach a desired configuration ($\mathcal{C}$) by adjusting the pressure regulators through a PD controller. The blue lines show the flow of the open-loop control, where the inverse kinematics model is used to determine the required pressure inputs without feedback.

Spatial configuration estimation of the origami manipulator. The origami manipulator consists of multiple extended OCMs, as shown in Figure 1(A), each undergoing complex deformation under applied forces and moments. Unlike conventional rigid-link manipulators, actuator lengths in pneumatic continuum manipulators are not directly controlled, requiring an IK formulation to determine the configuration from input pressures (P) when external load (τ_{ext}) is applied.

Each extended OCM is composed of three serially stacked OCMs in a column, with three such columns positioned in parallel at 120° intervals. Due to the PCC assumption, all OCMs in the same column share the same internal pressure (P), the same strain response, and the same bending angle (ϕ_C), ensuring uniform deformation across the manipulator.

Following the inverse mapping formulation of equations (24) and (25), the configuration of the origami manipulator is derived by extending the kinematic model of a single OCM while accounting for load propagation in the stacked structure.

Force and moment equilibrium for the origami manipulator. Each extended OCM is composed of three

actuators positioned at 120° intervals around the central backbone. The deformation of each actuator depends on the applied external force (τ_{ext}), the internal pressure (P), and the constraints of the neighboring module.

In Figure 4(C), the total force equilibrium at the tool center point (TCP) for the j-th floor in the manipulator is given by:

$$F_{z1,j} + F_{z2,j} + F_{z3,j} = F_z + W_j + \sum_{k=j+1}^{3} W_k, \tag{27}$$

where F_z represents the external force applied at the top plate, and W_j accounts for the gravitational weight contribution from the current and upper floors. The moment equilibrium equations, considering the external moments M_x and M_y, are formulated as:

$$\begin{aligned} M_x &= d(F_{z2,j}\sin 120° + F_{z3,j}\sin 240°), \text{ and} \\ M_y &= d(F_{z1,j} - F_{z2,j}\cos 120° - F_{z3,j}\cos 240°). \end{aligned} \tag{28}$$

The torsional moment M_z is considered zero due to the high torsional stiffness of the origami structure (Santoso and Onal 2021). Then, the forces for the individual actuators can be solved as:

$$\begin{aligned} F_{z1,j} &= \frac{F_z + W_j + \sum_{k=j+1}^{3} W_k + \frac{M_y}{d} + \frac{M_x}{\sqrt{3}d}}{3}, \\ F_{z2,j} &= \frac{F_z + W_j + \sum_{k=j+1}^{3} W_k - \frac{2M_x}{\sqrt{3}d}}{3}, \text{ and} \\ F_{z3,j} &= \frac{F_z + W_j + \sum_{k=j+1}^{3} W_k - \frac{M_y}{d} + \frac{M_x}{\sqrt{3}d}}{3}. \end{aligned} \tag{29}$$

These equations define how the load distribution affects the individual external forces within a single OCM when integrated into an entire manipulator.

Bending and strain estimation using LUTs. To determine the general configuration of the manipulator, the bending angle (Φ_c) and the bending direction (θ_c) for each OCM must be calculated. The total bending moment is:

$$M = \sqrt{M_x^2 + M_y^2}. \tag{30}$$

Applying the precomputed LUT for bending, the deformation parameters are estimated as

$$\theta_C = \mathbb{F}_{\mathbb{B}}^{\dagger}(M, S_C), \text{ and } \phi_C = \tan^{-1}\left(\frac{M_y}{M_x}\right) \tag{31}$$

where S_C is the backbone length of a single extended OCM. Since all three OCMs in an extended OCM deform identically, the total manipulator bending angle is

$$\theta_{\text{total}} = 3\phi_C. \tag{32}$$

Similarly, the strain in each OCM is obtained from the inverse mapping function:

$$\epsilon_{ij} = \mathbb{F}_{\mathbb{A}}^{\dagger}(F_{z,ij}, P_i). \tag{33}$$

Actuator length estimation for the origami manipulator. Once the strain values are retrieved from equation (33), the individual actuator lengths for the j-th floor are computed as

$$\begin{aligned} l_{1j} &= S_C + \epsilon_{1j} l_0 + d(\cos\theta_C - 1), \\ l_{2j} &= S_C + \epsilon_{2j} l_0 + d(\cos(\theta_C - 120°) - 1), \text{ and} \\ l_{3j} &= S_C + \epsilon_{3j} l_0 + d(\cos(\theta_C - 240°) - 1). \end{aligned} \tag{34}$$

These equations incorporate the effects of both axial and bending deformations, ensuring that the actuator length is correctly determined and applied in equation (26) to estimate the resultant tip position and orientation.

Pressure-controlled configuration estimation. Extending the inverse mapping method from a single OCM to the entire manipulator, we consider the combined effects of external forces and moments on the stacked OCMs. The configuration parameters, including actuator lengths (l_i), can be determined using the inverse function:

$$\mathcal{C} = f_{OCM}^{\dagger}(P, \tau_{ext}). \tag{35}$$

Here, τ_{ext} represents the total external load, including the gravity and the externally applied forces.

For a manipulator consisting of multiple extended OCMs in series, the LUT method is applied iteratively, accounting for load propagation from the top plate downwards. The required pressure to maintain a specific configuration can be calculated as:

$$\widehat{P} = f_{OCM}^{\dagger\dagger}(\tau_{ext}, \mathcal{C}), \tag{36}$$

where $f_{OCM}^{\dagger\dagger}$ represents the inverse function that estimates pressure based on external forces and target configurations. This function provides a pathway for real-time pressure control to achieve the desired configuration of the manipulator.

Experiment setup

Characterization of the origami cylinder module

Experiments were proposed to examine the kinematics of the constructed OCMs and to validate the accuracy of the model. Since the linear and the bending kinematics were

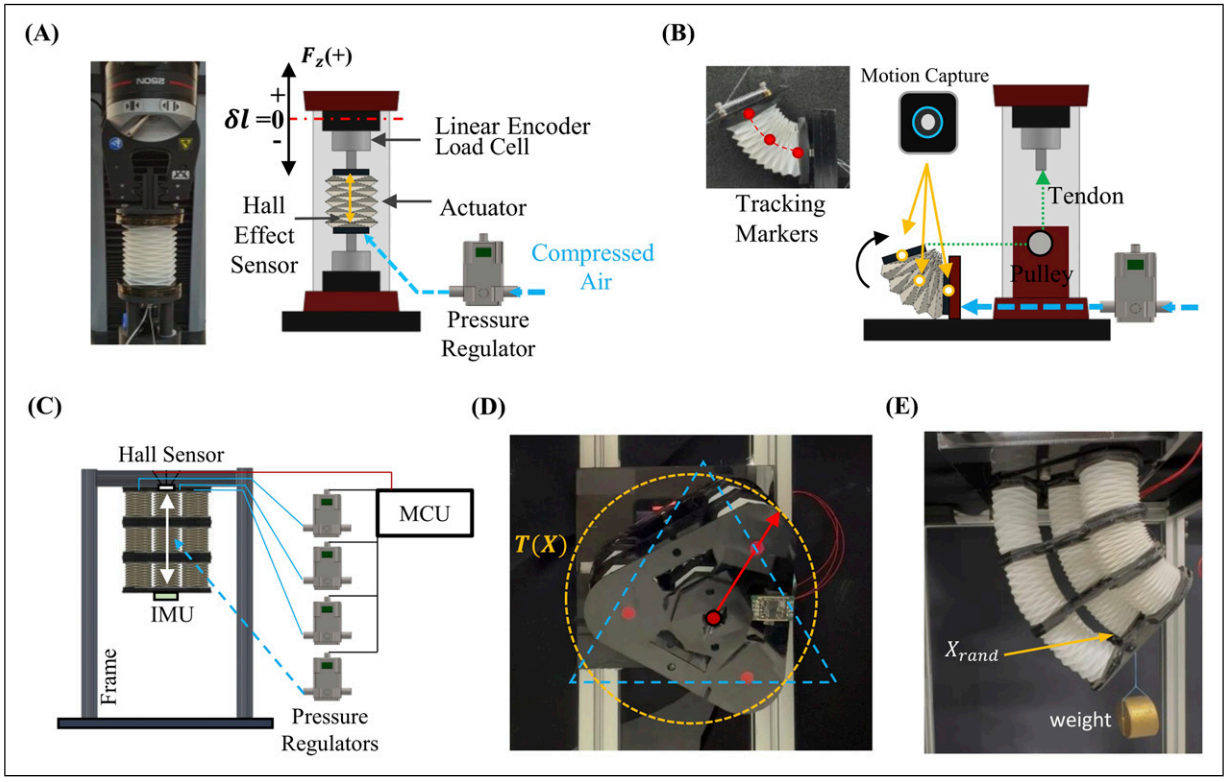

Figure 5. (A) Experimental setup for loading-unloading test using a tensile tester. The input pressure was controlled using a pressure regulator. (B) Experimental setup for bending experiment, using a pulley system to exert a moment on the origami cylinder. Three markers attached to the side of the OCM were tracked using a motion capture system. (C) Experimental setup for controlling the origami manipulator. (D) Circular and triangular trajectories to be tracked by the manipulator with position control. (E) Position control of random tip position control with a vertical load applied at the tip.

decoupled through the derivation, separated experiments were performed to measure the axial deformation and the pure bending of the OCMs.

For axial deformation, the normal force (F_z) and the length of the actuator (l) were measured to characterize the response under a constant pressure input and an external load. Figure 5(A) shows the force and the strain data collected using a tensile tester (34SC-1, Instron), while the pressure input (P) was controlled by a pressure regulator (ITV2030-212cl, SMC). The head of the tensile tester was programmed to move at a rate of 0.01 mm/s, ensuring a quasi-static condition. The pressure varied from 0 kPa to 30 kPa with an increment of 2 kPa, resulting in 16 distinct isobaric force-strain curve profiles. The initial length (l_0) of an individual actuator was set to 40 mm, with the strain spanning from -60% to 60%, ensuring operational durability without causing permanent damage to the origami structure.

The setup for the bending experiment is shown in Figure 5(B), where a tendon cable was attached at the tip of the actuator to exert a bending moment. The actuator entered a bending state when the cable was pulled for a certain distance from the neutral axis. Moment-angle curves were obtained while maintaining the same length of the neutral axis (s). In the absence of external loads, the pressure within the origami chamber was adjusted to define the initial length (l_0) prior to bending. The actuator varied from the fully compressed state, i.e., $l = 20$ mm ($\epsilon = -0.6$), to the fully extended state, that is, $l = 80$ mm ($\epsilon = 0.6$), with a 3 mm increment, yielding 21 bending profiles. The range of the bending angle was experimentally determined to remain within the feasible ROM of the actuator. The bending sequence was video-recorded to track the markers placed on the actuator, and the curvature and the bending angle were tracked using a motion capture system (OptiTrack, NaturalPoint). The error from the motion capture system and the accumulated propagation error were summarized in Table 2. Details on the calibration of the motion capture system are provided in Supplemental Information–E. The moment was indirectly calculated using the moment arm length and the force data from the tensile tester.

The origami cylinder structure exhibited converging force-displacement curves under repetitive actuation,

Table 2. Summary of modeling and control results across different experimental scenarios.

Metrics	Result
OCM characterization	$\mathbb{F}_A$: [e_F : 7.4% (0.77 N), e_{hyst} : 4.7% (0.48 N)] $\mathbb{F}_B$: [e_M : 18.0% (0.014 Nm), e_{hyst} : 5.9% (0.005 Nm)]
Origami manipulator ROM	ROM (l_{max} = 157.79, θ_{max} = 0.788) RMSE$(X, \widehat{X})$: 2.15% (3.45 mm), RMSE$(q, \widehat{q})$: 2.67% (0.028 rad)
Trajectory tracking	Triangle: [OL: 15.30 mm, CL: 7.22 mm] Circle: [OL: 7.62 mm, CL: 5.54 mm]
Position control with the external load	Random 10 points: [OL: 14.29 mm, CL: 5.86 mm] Average rise time = 3.48 s, settling time = 7.32 s
Orientation regulation with dynamic external load	RMSE$(q, \widehat{q})$: 3.15% (0.033 rad) Average rise time: 1.21 s, settling time: 2.55 s

primarily due to the stiffness degradation from wear along the crease lines, as reported in a prior study (Yasuda et al., 2013). Accordingly, the origami cylinder used for the specimen underwent 400 loading and unloading cycles to achieve a stable curve behavior. As shown in Figure 6(A) and (B), both linear and bending actions produced convergent curves, indicating consistent performance during different tests.

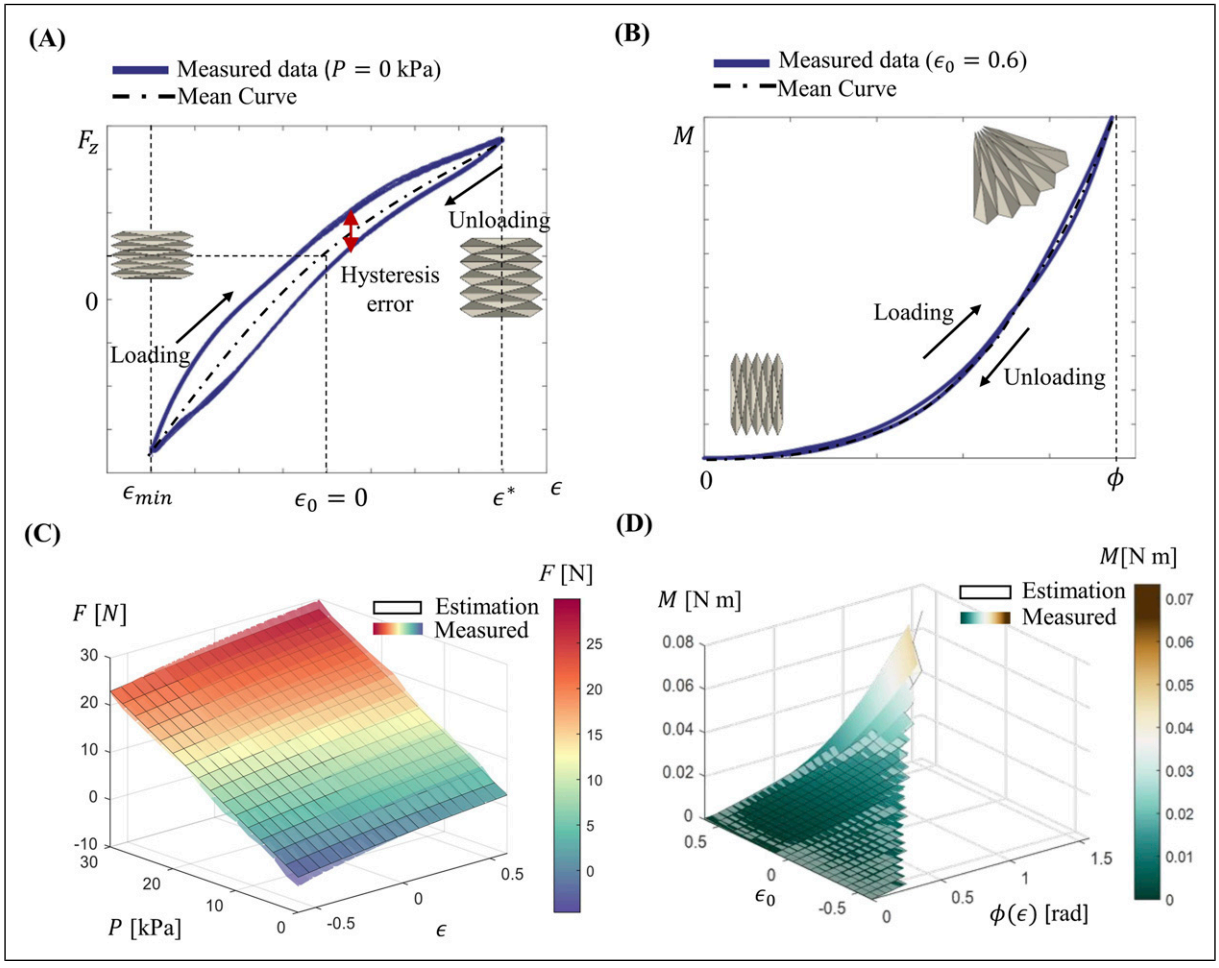

Figure 6. (A) Measured data of the cyclic test for linear deformation of the OCMs, showing the force-strain curves when no input pressure was applied. (B) Measured data from the cyclic test for bending deformation, with an initial strain (ϵ_0) of 0.6. (C) Grid plot visualizing the 3D relationship of force, pressure, and strain. Experiments were conducted with 16 different pressure levels with an increment of 2 kPa, within the strain range of −60% to 60%. Solid lines represent the forces estimated by the model, while the filled surfaces show the measured data. (D) Moment and bending angle curves for 16 different initial strains (ϵ_0) of the single layer. The initial strains (ϵ_0) were adjusted through 16 steps of pressure inputs, consistent with the linear deformation experiments. Solid lines indicate the moments estimated by the model, while the filled surfaces show the measured data.

Control task implementation in the soft manipulator

Continuing from the previous sections, several experiments were conducted to evaluate the performance of the OCM-integrated manipulator, and the experimental setup is shown in Figure 5(C). To control the manipulator, the three types of sensors were utilized, and three origami cylinders were independently controlled by three pressure regulators. Inertial measurement units (IMU) (ebimu-9dofv5-r3, E2box) determined the orientation of the top moving plate S relative to the fixed base frame B, and Hall-effect sensors within each chamber provided estimates of the lengths of the bent actuators after calibration. Using both the IMU and the Hall effect sensors, it was possible to measure the orientation of the frame $\{S\}$ and the length of the backbone of the manipulator (s_c). The detailed hardware setup is also shown in Supplemental Information–D.

Employing the PCC assumption for the continuum manipulator allowed us to determine a unique position at the tip of the frame $\{S\}$, as explored in prior research (Jones and Walker, 2006). Throughout the experiments, both the position ($\vec{X}$) and the orientation (n_X, n_Y, and n_Z) of the tip of the manipulator were systematically measured. The task operation can also be viewed in Supplemental Video 1.

The following experiments were conducted to evaluate the performance of the origami manipulator and the accuracy of the derived model.

Range of motion test. The first experiment aimed at monitoring the centroid position of the frame S, employing various combinations of pressure inputs to explore the accessible space of the designed manipulator. Each test iteration followed 16 pressure steps, mirroring the axial deformation experiments. With the manipulator featuring three DOFs, the total combination was $16^3 = 4096$ points. The estimated positions from the FK ($\vec{X}$) and the experimentally measured points ($\widehat{X}$) were compared using root-mean-square error (RMSE). Also, the orientation error was similarly calculated by comparing the Euler angles (n_X, n_Y, and n_Z). The actual position and the orientation of the tip were measured using the IMUs and the Hall-effect sensors.

Trajectory tracking tasks. The second experiment involved trajectory tracking, with two time-dependent trajectories of a triangle and a circle, providing the references for open-loop control (see Figure 5(D)). When the targeting trajectories were predefined, the required profiles of each actuator was obtained using the function, shown in equation (26). If the targeting time variance of each length is obtained, the input pressure profiles can be derived using the relation between the pressure input and the configuration from the equation (35). For comparison, we also conducted the proportional-derivative (PD)-control using the embedded sensors.

Position control with external load. The last experiment was the position control using the kinematic model while the external load was applied. As shown in Figure 5(E), a 250 g weight nearly equivalent to the total mass of the manipulator (W_m = 230 g) was attached at the tip of the manipulator during actuation to check the performance with the payload. 10 random coordinates inside the ROM were selected and scheduled to move continuously. The input pressure profiles of the three actuators were designed to make the tip position of the manipulator to track the selected positions. Given the objective to verify the accuracy of the programmed model in reaching the target positions, a settling time of 10 seconds, enough for entering a steady state, was allowed.

Adaptation to the dynamic loading. To evaluate the force feedback and the configuration control capabilities of the origami manipulator, a dynamic loading scenario was tested. Using the model derived in equation (22) for each OCM composing the manipulator, the external force was estimated. While estimating the external force, a specific configuration, such as the tip position or the orientation of the upper frame {S}, was controlled. The objective of the experiment was to maintain the predefined configuration as incremental weights were added. As shown in the setup in Figure 5(E), the external load was applied at the center of the frame {S}, and closed-loop control was implemented to achieve this task.

Measuring the maximum load. The manipulator was also tested with a vacuum pressure input to test how much weight it can lift by contracting the OCMs. The results are summarized in Table 3 and provided in Supplemental Video 1.

Various applications

To highlight the versatility and the potential practical applications of the proposed OCMs, we present example configurations and their operations.

Origami gripper. The OCMs can be utilized to construct an adaptive origami-based gripper, as shown in Figure 8(A). This gripper leverages the flexibility and the compliance of the OCMs to conform to various shapes and sizes of target objects. The combination of axial and bending deformation allows the gripper to handle delicate objects while maintaining enough stiffness to apply the grasping forces. Such a system has potential applications in areas that require delicate manipulation, such as handling fragile items in unstructured environments.

Origami continuum robot. The OCMs can also be extended to form a two-segment continuum robot, as shown in Figure 8(B). By connecting multiple OCMs in series, the manipulator is capable of performing complex motions, such as bending and reaching into constrained spaces. The

Table 3. Comparative Analysis of Soft Robotic Manipulators.

Author (Year)	Control	Model	Volume [mm]	ROM [mm, deg]	Payload [N]	Pressure [kPa]	Weight [g]	Error [%]
Greer et al. (2017)	CL	Sensory	38 × 38 × 420	400 × 400 × 300	2	10.38	–	5
Hao et al. (2018)	CL	FK	L: 625, R: 75	–	5	250	–	4.09
Zhang et al. (2019)	OL	FK	L: 300, R: 39	Angular: 90	24.56	100	70.2	1.21*
Huang et al. (2022)	OL	IK	40 × 40 × 200	300 × 300 × 400	0.6	200	–	2.89
Toshimitsu et al. (2021)	OL	PCC	–	200 × 200 × 100	1.17	–	–	4.23*
Robertson et al. (2021)	OL	Geometric	L: 45	Linear: 45, Angular: 42.5	2	60	56	–
Shen et al. (2021)	CL	Sensory	L: 114, R: 54	Angular: 78	2.3	100	–	3.37*
Zou et al. (2021)	CL	Sensory	L: 800, R: 15	Linear: 800, Angular: 120	2	103	–	–
Liu et al. (2022)	OL	PCC	L: 2300, R: 100	–	–	100	5000	–
Zaghloul and Bone (2023)	CL	Sensory	L: 101.6, R: 50.8	Linear: 76.2	440	185	72	–
Fan et al. (2024)	CL	Sensory	L: 60	40 × 40 × 40	2000	80	–	5
Mak et al. (2024)	OL	-	L: 97	Angular: 94.7	25.4	140	43	–
Ku et a. (2024)	CL	FK, IK	L: 234.5, R: 80	Linear: 102, Angular: 70.4	20	80	1100	1.07*
Zhang et al. (2024)	OL	FK, IK	L: 430.7	–	0.302	125	355.2	7.8
This work (OCM)	CL	FK, IK	L: 155, R: 52.5	160 × 160 × 80, Angular: 60.4	10	40	238	2.15*

Cited Papers: (Greer et al., 2017, Hao et al., 2018, Zhang et al., 2019, Huang et al., 2022, Toshimitsu et al., 2021, Robertson et al., 2021, Zou et al., 2021, Shen et al., 2021, Liu et al., 2022, Zaghloul and Bone, 2023, Fan et al., 2024, Mak et al., 2024, Ku et a., 2024, Zhang et al., 2024), The position errors marked with * are the errors calculated using the methods we defined in equation (41).

robot can also be augmented with an end effector, such as a gripper for object manipulation, making it suitable for applications in inspection, exploration, or soft robotic navigation in unstructured environments. The derivation of the kinematics of this two-segment robot is similar to the process described in the manipulator model in the Model of the Origami Manipulator section, but it additionally accounts for the interaction force and moment from the neighboring segment. The formulation is summarized in Supplemental Information–F. In addition, the demonstration of these systems, along with task execution and performance, is presented in the Results section and the Supplemental Video 2.

Results

Validation of the OCM kinematics model

The experiments were designed to validate the models derived by equations (9) and (21). Initially, observations of linear and bending deformations were made without pressure input, as shown in Figure 6(A) and (B). These figures show characterization curves derived directly from the raw data. In Figure 6(A), the axial force value F_z is plotted against the calculated strain ϵ of the OCM, with the strain range conservatively set to $\epsilon \in [-0.6, 0.6]$ to avoid extreme deformation or damage. This setting resulted in a noticeable hysteresis error between the loading and the unloading curves, attributed to the hyperelastic nature of the origami cylinder. The hysteresis error, defined as the percentage difference between the loading (F^+) and the unloading forces (F^-) relative to the maximum force observed, is given by

$$e_{hyst} = \frac{F_z^+ - F_z^-}{\max(F_z)} \times 100\ (\%). \tag{37}$$

To align with the modeling equations, the mean curves from both loading (M^+)and unloading (M^-) data for force and moment was determined as

$$\overline{F_z} = \frac{F_z^+ + F_z^-}{2}, \quad \text{and } \overline{M} = \frac{M^+ + M^-}{2}, \ \textit{respectively}. \tag{38}$$

In the bending experiment, the range of the bending angle was influenced by the initial strain of the cylinder, in line with equation (13). For example, Figure 6(B) demonstrates a bending range up to 1.5 radians, identified as the limit to avoid damage. The extended characterization curves for the linear deformation are shown in Figure 6(C). As the input pressure level was changed, multiple characterization curves

were obtained. All points corresponding to a specific axial force (F_z), strain (ϵ), and pressure (P) are plotted. The estimation values using equation (9) are also overlaid on the measured data to highlight the discrepancies. Since the actual experiments were conducted with discrete pressure values, the data points are visualized in a color-filled grid to indicate this, although the model represented by equation (9) could be plotted as a continuous surface. The force was estimated at each point, denoted as $\widehat{F}_z$ and is shown with a gradient color in Figure 6(C). The force estimation error was calculated as

$$e_F = \left| \frac{\widehat{F}_z - F_z}{F_z} \right| \times 100 \ (\%), \tag{39}$$

which showed an error of 7.4% overall, 0.77 N in force. The error tends to increase at higher pressures above 20 kPa, where the error rate was 13.7% in the worst case. In addition, the average hysteresis error was 4.7% in the axial force.

For the bending case, the extended curves measured by changing the initial strain values are shown in Figure 6(D). A notable point is that the feasible bending range was determined by the initial strain; the larger the strain, the wider the range of bending angles possible. This observation aligns with the modeling, which sets geometric constraints based on the initial strain ϵ_0. Hence, it can be concluded that the initial strain before bending can serve as an indicator of the allowable bending range. The errors related to the moment were calculated in the same manner as in the axial case. The average moment estimation error was 18%, equivalent to 0.014 Nm in moment. Furthermore, the average hysteresis error was 5.9%. The errors tended to increase with larger initial strains, where a wider ROM was observed for the bending angle.

Task implementation results

The proposed manipulator in this study has three DOFs and was actuated using all possible combinations of pressure inputs. These results were compared with analytic estimations using equations (26) and (35). Initially, the reachable space of the manipulator was tested, as shown in Figure 7(A). The position and the orientation errors between the measured data and the estimations were calculated for each combination of pressure inputs ($P_1 \sim P_3$). The manipulator operated within the expected ROM, with an average RMSE for the position between $\overrightarrow{X}$ and $\widehat{X}$ of less than 8.2 mm. However, several outlier points were observed at high-pressure inputs, with the maximum error of 24.5 mm.

To better represent the position error relative to the overall workspace, the position error was also normalized using the ROM-based percentage error. The ROM-based error was calculated using

$$l_{max} = \sqrt{\delta_x^2 + \delta_y^2 + \delta_z^2}, \tag{40}$$

where δ_x, δ_y, and δ_z represent the total workspace ranges in each axis. The position error is then normalized as

$$e_{\mathrm{ROM,n}} = \frac{|\overrightarrow{X} - \widehat{X}|}{l_{max}} \times 100 \ (\%), \tag{41}$$

where $|\overrightarrow{X} - \widehat{X}|$ represents the absolute positional error. This normalized error gives a clearer indication of the manipulator's performance relative to its workspace. The average RMSEs for the orientation errors were replaced with quaternion-based errors for improved accuracy. The quaternion error was calculated using

$$e_q = 2 \cdot \arccos(|q_{\mathrm{m}} \cdot q_{\mathrm{e}}|), \tag{42}$$

where q_{m} and q_{e} are the quaternions representing the measured and the estimated orientations, and $\cdot$ denotes the dot product. This method provides a more holistic measurement of the orientation error compared to the separate analyses of n_X, n_Y, and n_Z. In the same way, the normalized quaternion error was calculated by dividing the error by the maximum bending angle $\theta_{\max}$:

$$e_{q,\mathrm{n}} = \frac{e_q}{\theta_{\max}} \times 100 \ (\%). \tag{43}$$

Here, regions with extreme deformations caused an increase in the overall average position estimation error. To better assess precision in moderate deformation regions, the reduced ROM was set as x-y coordinates in $-50 \sim 50$ mm, and the z-coordinate ranged from $70 \sim 140$ mm. The errors of all the experiments are summarized in Table 2.

In the trajectory tracking tasks, two trajectories on an x-y plane with a constant z coordinate were provided as references, included within the measured ROM. The reference trajectories $T(\overrightarrow{X})$ were defined as position functions over time. The position error was calculated between the model estimation $T(\overrightarrow{X})$ and the measured data $T(\widehat{X})$ at the corresponding times. When estimating the positions using the model, the pressure input for each OCM was inversely calculated using equation (35), assuming the target trajectories were given under zero external load. This control strategy, using exclusively the model, is considered as open-loop control (OL) and shown in the results Figure 7(B). Alongside model validation in the open-loop control, the closed-loop control performance using the attached IMUs and the Hall-effect sensors was also evaluated. In this case, triangular and circular trajectories were selected. For the triangular trajectory, the average RMSE position errors for the open-loop and the closed-loop controls were 15.30 mm and 7.22 mm, respectively. For the circular trajectory, RMSE errors were 7.62 mm and

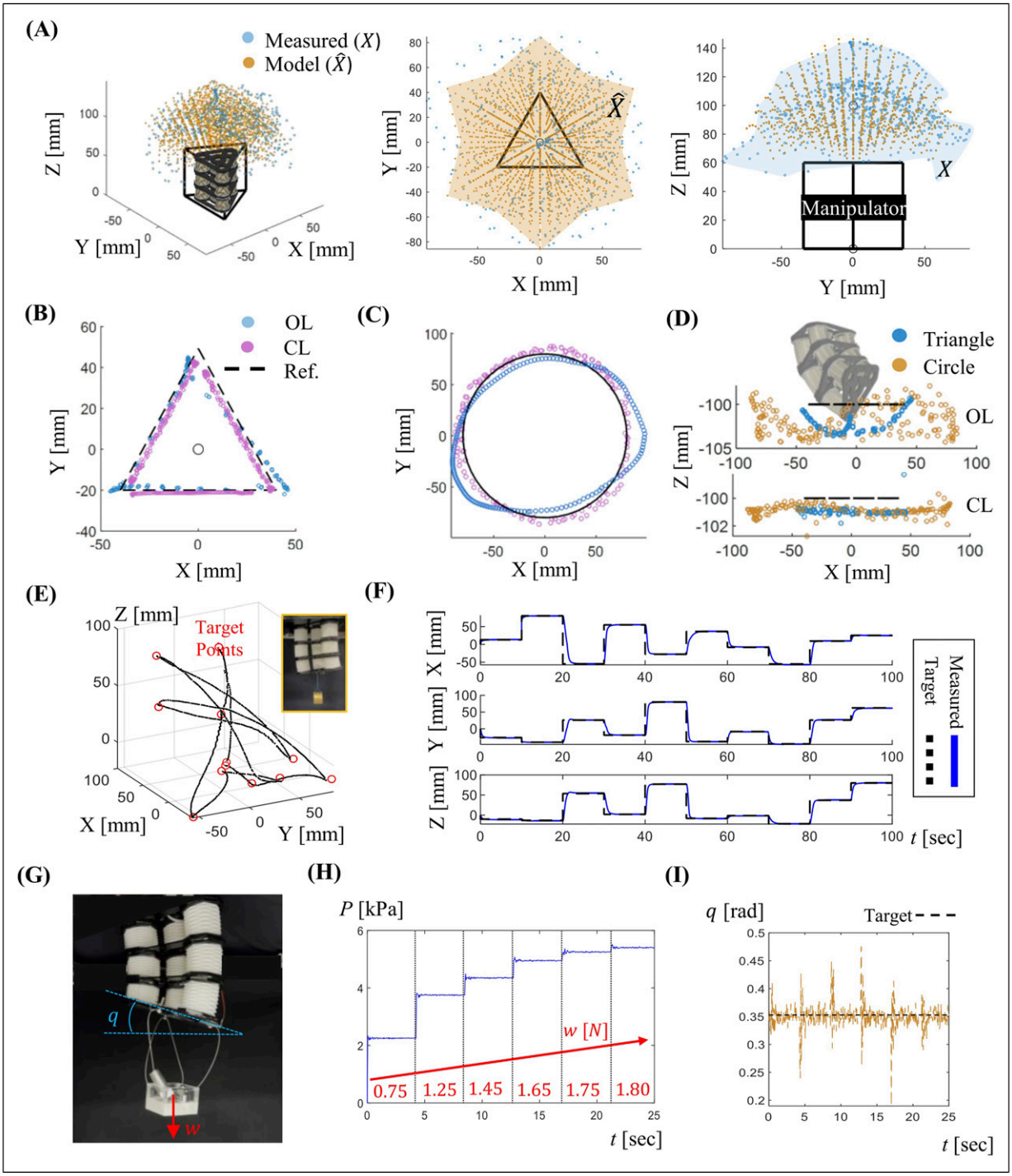

Figure 7. (A) Workspace analysis with all combinations of pressure inputs, comparing the model predictions with the actual measurements. (B) Result of triangular trajectory tracking conducted on a $z = -100$ mm plane. (C) Result of circular trajectory tracking control performed on a $z = -100$ mm plane. (D) z-axis positions measured during both tracking tasks, comparing the model-based open-loop (OL) control with the closed-loop (CL) control that uses the embedded IMU and the Hall-effect sensors. (E) 10 target points with random selections in red circles and the actual trajectories of the manipulator's tip. 10 seconds were allowed to reach each goal position, allowing the entire task completion time of 100 seconds. (F) Position control results in three axes, demonstrating the manipulator's performance in reaching the targets. (G) Experimental setup for position holding as the load increased over time. The manipulator maintained the target angle q throughout the experiment while the load increased from 0.75 N to 1.80 N over 25 seconds. (H) Pressure input profile as the external load increased. (I) Result of the quaternion angle during the task maintained by the manipulator around the target value.

5.54 mm, respectively. The results of both tasks are plotted in Figure 7(B)–(D). For both trajectories, the open-loop control required 10 seconds per cycle to complete the tracking tasks, as the controller utilized the programmed model, thus spending the same amount of time in all trials. However, in the closed-loop control, due to the PD control of the error, the time varied in each trial but typically converged within approximately 5 s and 10 s for the triangular and the circular trajectories, respectively.

In the position control task with an external load, the manipulator successfully moved to 10 randomly selected target points, even with external loads applied during operation. The points and recorded trajectories measured from the manipulator are shown in Figure 7(E), and the error for each coordinate is plotted in Figure 7(F). Over the sufficient time for task implementation of 10 s at each target point, the position errors were measured as 5.6 mm, 4.7 mm, and 7.3 mm in the x, y, and z directions, respectively, with an average error of 5.86 mm in the 3D space. Additionally, the rise time and the settling times were measured at each target point to assess the performance, averaging 3.4 s and 7.3 s, respectively. When using the prediction model (open-loop), the errors were similar to those from the trajectory tracking test, with an average distance error of 14.29 mm.

In the force control task, where the manipulator maintained its position as external loads were gradually increased, an error of 3.15% was observed in regulating the orientation (q), corresponding to 0.033 rad. The dynamic performance was better than in the previous position control tasks, with average rise and settling times of 1.21 s and 2.55 s, respectively.

Applications

The demonstration results of the continuum robot are shown in Figure 8(E) and (F). Supplemental Video 2 also presents the task execution of the origami gripper and the continuum robot in action, picking up a target object at a predefined position. The task required control of both the orientation and the position of the end-effector to avoid collision with the object before positioning the gripper for stable gripping. The reaching process was divided into five continuous steps, gradually approaching the target object. Once the object was reached, the gripper was actuated to grasp it.

Six extended OCMs were used, with the backbone lengths tracked by the Hall-effect sensors, while two IMUs in each trunk measured the orientations. The predefined positions and orientations for each step were set before the task and controlled using a PD control loop, as introduced in Figure 4(C). Figure 8(E) shows the position tracking results in the x, y, and z coordinates, and Figure 8(F) displays the measured orientation during the tasks. The continuum robot successfully reached and grasped the target object within 25 s.

Discussion

The experimental results verify the feasibility and the effectiveness of the proposed soft continuum manipulator, which leverages OCMs with proprioceptive functionality. Experiments on the linear and the bending deformation modes of the OCM confirmed the accuracy of the model. Moreover, integrating proprioceptive OCMs into the soft continuum manipulator demonstrated the potential for practical applications.

The validation of the OCM model showed low errors in estimating both force and moment, indicating the possibility of practical implementation of the Yoshimura pattern-based origami actuator in real-world settings. The errors however rapidly increased under extreme conditions, such as at high pressures or strains, and hysteresis was also observed in both force and moment measurements, which may have been caused by several reasons, such as variations in the material properties and manufacturing tolerances from manual fabrication. While the model simplifies the complexity in the analysis that typically uses FEA, it may not capture various nonlinear behaviors. Nevertheless, within a defined ROM for both OCMs and the manipulator, the model proved to be useful.

When assembled into a larger system, the OCMs demonstrated the capability of reaching diverse positions and making different orientations with precision. Although the average errors within the ROM tasks were modest, the outliers at high pressure inputs highlighted the kinematic nonlinearities, particularly over-actuation at extreme pressure levels, which affected the accuracy of the prediction model and sometimes violated the PCC assumptions. The trajectory tracking task showed the efficacy of the model in open-loop control, and the accuracy was even increased with closed-loop control, suggesting its potential to improve the performance in practical implementations. Notably, in tasks involving payloads, the manipulator was able to maintain the high accuracy, with decreased errors and relatively short settling times.

Table 3 compares our proposed origami-based soft pneumatic manipulator system with state-of-the-art systems. Our approach introduces several distinct advantages derived from our novel modeling and design strategies. Unlike existing systems that utilize origami cylinders primarily as structural shells with separate actuators, such as pneumatic muscles or SMA wires, our Origami Cylinder Modules (OCMs) serve simultaneously as the structural framework and the pneumatic actuator chambers. This integrated design significantly reduces complexity and weight, enhancing the manipulator's overall agility and responsiveness.

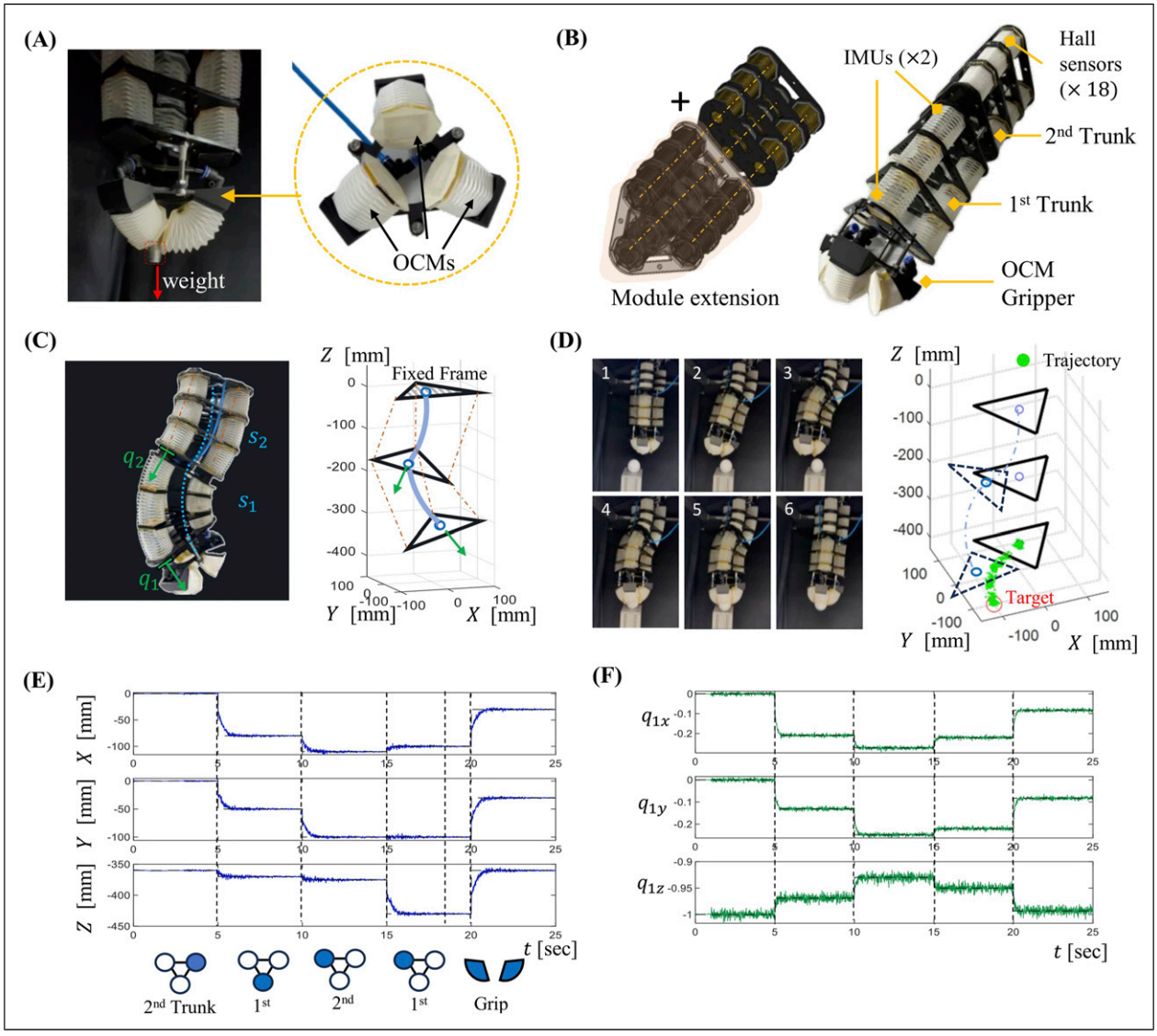

Figure 8. (A) Soft gripper prototype composed of three bending OCMs. One side of each OCM is fixed to realize to the module's bending motion when pressurized, with all three OCMs oriented toward the center of the gripper. (B) Extended manipulator segments as a continuum robot with the gripper installed at the end. IMUs are installed in each trunk segment, and a Hall-effect sensor is embedded in each OCM. (C) Configuration estimation of two trunks using embedded proprioceptive sensors. (D) Object picking task using the continuum robot using the open-loop control. A total of five different steps were planned to reach the predefined object location and pick up and place the object in the end. (E) Position control result of the task implemented by the continuum robot (top) and five input commands during the task (bottom). (F) Orientation changes following the five input steps, measured by the IMU sensor on the first trunk.

Our simplified kinematic model explicitly incorporates internal pressure inputs, volumetric deformation, and virtual work, extending conventional strain-energy-based geometric approaches. By establishing explicit mapping functions based on extensive experimental data, our model enables efficient real-time forward and inverse kinematics computations. This modeling strategy provides scalability, seamlessly transitioning from single OCMs to modular manipulators and multi-segment continuum robots without requiring additional assumptions or rigid-link approximations.

Additionally, the integration of proprioceptive sensing mechanisms, specifically Hall-effect sensors for length measurement and IMUs for orientation, significantly enhances real-time closed-loop control capabilities. This embedded sensing strategy allows accurate manipulation and robust performance in complex operational tasks, such as precise trajectory tracking and dynamic payload handling, without sacrificing system simplicity.

Overall, this combination of an integrated pneumatic-actuated origami design, a scalable and simplified kinematic modeling approach, and embedded proprioceptive feedback

positions our system uniquely among soft pneumatic manipulators, offering substantial improvements in control efficiency, payload capacity relative to self-weight, and adaptability to complex manipulation tasks.

Future work could include the exploration of the dynamic characteristics of the system, leveraging the numerically derived models and equations for differentiation. Following the approaches in previous studies (Kidambi and Wang 2020; Zhang et al., 2023), incorporating derivatives of pressure-to-configuration relationships could yield a dynamic model that includes the velocity and acceleration terms, offering a comprehensive analysis of the Yoshimura cylinder used as a pneumatic actuator.

Another area of future work will be incorporation of tactile or force sensors into the actuation modules for detecting contacts from the surroundings. Different sensing mechanisms, such as microfluidic (Park et al., 2012; Yang et al., 2020), capacitive (Jung et al., 2024; Weichart et al., 2021), or fiber-optic sensors (Yi et al., 2023), can be employed, combined with machine learning algorithms. In this way, the robotic arm will be more interactive with the environments including humans (Kim et al. 2023) or robust in rejecting disturbances (Kim et al. 2023).

Conclusion

This study introduced a soft continuum manipulator based on modular origami cylinder modules, using a kinematic model rooted in the Yoshimura origami pattern. The validated model effectively predicted the linear and the bending deformations under pneumatic actuation, demonstrating its practicality in real-world applications. While errors increased in extreme conditions, the system showed a reliable performance within its normal range, with low errors in estimating both force and moment.

The lightweight origami structure enabled the manipulator to carry high loads relative to its weight, allowing for faster movement and a large ROM. Embedded proprioceptive sensors enhanced control accuracy, especially in closed-loop control tasks. Comparison with state-of-the-art soft robots demonstrated the competitive performance in load capacity, simplicity and precision of the prediction model.

While challenges remain, particularly under extreme conditions, this work bridges theoretical modeling and practical applications in soft robotics, laying the foundation for future research into dynamic modeling and further origami-inspired designs.

ORCID iDs

Taehwa Hong https://orcid.org/0000-0003-1105-1391
Jinkyu Yang https://orcid.org/0000-0003-1547-0219
Yong-Lae Park https://orcid.org/0000-0002-2491-2114

Funding

The author(s) disclosed receipt of the following financial support for the research, authorship, and/or publication of this article: This work was supported in part by the National Research Foundation (Grant No. RS-2024-00416938) and in part by the Technology Innovation Program (Grant No. 00423940), funded by the Ministry of Science and ICT and the Ministry of Trade, Industry and Energy of Korea, respectively. J.Y. also acknowledges the support by the National Research Foundation grants funded by the Korea government [Grants No. 2023R1A2C2003705 and 2022H1D3A2A03096579].

Declaration of conflicting interests

The author(s) declared no potential conflicts of interest with respect to the research, authorship, and/or publication of this article.

Supplemental Material

Supplemental material for this article is available online.

References

Al Abeach LA, Nefti-Meziani S and Davis S (2017) Design of a variable stiffness soft dexterous gripper. *Soft Robotics* 4(3): 274–284.

Cai J, Deng X, Xu Y, et al. (2016) Motion analysis of a foldable barrel vault based on regular and irregular yoshimura origami. *Journal of Mechanisms and Robotics* 8(2): 021017.

Chen B, Shao Z, Xie Z, et al. (2021) Soft origami gripper with variable effective length. *Advanced Intelligent Systems* 3(10): 2000251.

Choi I, Yoon SJ and Park Y-L (2023) Linear electrostatic actuators with moiré-effect optical proprioceptive sensing and electroadhesive braking. *The International Journal of Robotics Research* 43(5): 646.

Chou C-P and Hannaford B (1996) Measurement and modeling of mckibben pneumatic artificial muscles. *IEEE Transactions on Robotics and Automation* 12(1): 90–102.

Dawood AB, Godaba H, Ataka A, et al. (2020) Silicone-based capacitive e-skin for exteroception and proprioception. In: Proceedings of the IEEE/ASME International Conference on Intelligent Robots and Systems (IROS), Las Vegas, NV, USA, 24 October 2020–24 January 2021, pp. 8951–8956.

Della Santina C, Katzschmann RK, Bicchi A, et al. (2020) Model-based dynamic feedback control of a planar soft robot: trajectory tracking and interaction with the environment. *The International Journal of Robotics Research* 39(4): 490–513.

Fan W, Wang J, Zhang Z, et al. (2024) Vacuum-driven parallel continuum robots with self-sensing origami linkages. *IEEE/ASME Transactions on Mechatronics* 29: 3370.

Filipov ET, Tachi T and Paulino GH (2015) Origami tubes assembled into stiff, yet reconfigurable structures and metamaterials. *Proceedings of the National Academy of Sciences of the United States of America* 112(40): 12321–12326.

Grazioso S, Di Gironimo G and Siciliano B (2019) A geometrically exact model for soft continuum robots: the finite element deformation space formulation. *Soft Robotics* 6(6): 790–811.

Greer JD, Morimoto TK, Okamura AM, et al. (2017) Series pneumatic artificial muscles (spams) and application to a soft continuum robot. In: Proceedings of the IEEE International Conference on Robotics and Automation (ICRA), Singapore, 29 May–03 June 2017, pp. 5503–5510.

Hao L, Xiang C, Giannaccini ME, et al. (2018) Design and control of a novel variable stiffness soft arm. *Advanced Robotics* 32(11): 605–622.

Ho-Le K (1988) Finite element mesh generation methods: a review and classification. *Computer-Aided Design* 20(1): 27–38.

Hong TH, Park S-H, Park J-H, et al. (2020) Design of pneumatic origami muscle actuators (POMAs) for a soft robotic hand orthosis for grasping assistance. In: Proceedings of the IEEE International Conference on Soft Robotics (RoboSoft), New Haven, CT, USA, 2020, pp. 627–632.

Huang J, Zhou J, Wang Z, et al. (2022) Modular origami soft robot with the perception of interaction force and body configuration. *Advanced Intelligent Systems* 4(9): 2200081.

Hunt GW and Ario I (2005) Twist buckling and the foldable cylinder: an exercise in origami. *International Journal of Non-Linear Mechanics* 40(6): 833–843.

Ji J, Luo Q and Ye K (2021) Vibration control based metamaterials and origami structures: a state-of-the-art review. *Mechanical Systems and Signal Processing* 161: 107945.

Johnson M, Chen Y, Hovet S, et al. (2017) Fabricating biomedical origami: a state-of-the-art review. *International Journal of Computer Assisted Radiology and Surgery* 12: 2023–2032.

Jones BA and Walker ID (2006) Kinematics for multisection continuum robots. *IEEE Transactions on Robotics* 22(1): 43–55.

Jung J, Park M, Kim D, et al. (2020) Optically sensorized elastomer air chamber for proprioceptive sensing of soft pneumatic actuators. *IEEE Robotics and Automation Letters* 5(2): 2333–2340.

Jung J, Lee E, Kim J, et al. (2024) Ultra-thin multi-modal soft sensor using liquid-metal thin-film deposition for enhanced human-robot interaction. *IEEE Robotics and Automation Letters* 9(6): 5269–5275.

Kang J, Lee S and Park Y-L (2023) Soft bending actuator with fiber-jamming variable stiffness and fiber-optic proprioception. *IEEE Robotics and Automation Letters* 8(11): 7344–7351.

Kaufmann J, Bhovad P and Li S (2022) Harnessing the multistability of Kresling origami for reconfigurable articulation in soft robotic arms. *Soft Robotics* 9(2): 212–223.

Kidambi N and Wang K (2020) Dynamics of Kresling origami deployment. *Physical Review E* 101(6): 063003.

Kim D, Kim S-H, Kim T, et al. (2021) Review of machine learning methods in soft robotics. *PLoS One* 16(2): e0246102.

Kim D, Lee S, Hong T, et al. (2023) Exploration-based model learning with self-attention for risk-sensitive robot control. *Npj Robotics* 1(7): 7.

Kim T, Lee S, Chang S, et al. (2023) Environmental adaptability of legged robots with cutaneous inflation and sensation. *Advanced Intelligent Systems* 5(1): 2370050.

Kshad MAE, Popinigis C and Naguib HE (2018) 3D printing of Ron-Resch-like origami cores for compression and impact load damping. *Smart Materials and Structures* 28(1): 015027.

Ku S, Song B-H, Park T, et al. (2024) Soft modularized robotic arm for safe human–robot interaction based on visual and proprioceptive feedback. *The International Journal of Robotics Research* 43(8): 1128.

Laschi C, Mazzolai B and Cianchetti M (2016) Soft robotics: technologies and systems pushing the boundaries of robot abilities. *Science Robotics* 1(1): eaah3690.

Lee J-G and Rodrigue H (2019) Origami-based vacuum pneumatic artificial muscles with large contraction ratios. *Soft Robotics* 6(1): 109–117.

Li S, Stampfli JJ, Xu HJ, et al. (2019), A vacuum-driven origami "magic-ball" soft gripper. In: Proceedings of the IEEE International Conference on Robotics and Automation (ICRA), Montreal, QC, Canada, 20-24 May 2019, pp. 7401–7408.

Li M, Pal A, Aghakhani A, et al. (2022) Soft actuators for real-world applications. *Nature Reviews Materials* 7(3): 235–249.

Liu K and Paulino GH (2016) Merlin: a matlab implementation to capture highly nonlinear behavior of non-rigid origami. In: *Proceedings of the IASS Annual Symposium 2016*, Tokyo, Japan, 26–30 September 2016, pp. 1–10. International Association for Shell and Spatial Structures (IASS).

Liu K and Paulino G (2017) Nonlinear mechanics of non-rigid origami: an efficient computational approach. *Proceedings. Mathematical, Physical, and Engineering Sciences* 473(2206): 20170348.

Liu S, Liu J, Zou K, et al. (2022) A six degrees-of-freedom soft robotic joint with tilt-arranged origami actuator. *Journal of Mechanisms and Robotics* 14(6): 060912.

Luo M, Skorina EH, Tao W, et al. (2017) Toward modular soft robotics: proprioceptive curvature sensing and sliding-mode control of soft bidirectional bending modules. *Soft Robotics* 4(2): 117–125.

Mak YX, Dijkshoorn A and Abayazid M (2024) Design methodology for a 3D printable multi-degree of freedom soft actuator using geometric origami patterns. *Advanced Intelligent Systems* 6: 2300666.

Martinez RV, Fish CR, Chen X, et al. (2012) Elastomeric origami: programmable paper-elastomer composites as pneumatic actuators. *Advanced Functional Materials* 22(7): 1376–1384.

Meloni M, Cai J, Zhang Q, et al. (2021) Engineering origami: a comprehensive review of recent applications, design methods, and tools. *Advanced Science* 8(13): 2000636.

Nishiyama Y (2012) Miura folding: applying origami to space exploration. *International Journal of Pure and Applied Mathematics* 79(2): 269–279.

Park Y-L, Chen B-r. and Wood RJ (2012) Design and fabrication of soft artificial skin using embedded microchannels and liquid conductors. *IEEE Sensors Journal* 12(8): 2711–2718.

Peraza-Hernandez EA, Hartl DJ, Malak Jr RJ, et al. (2014) Origami-inspired active structures: a synthesis and review. *Smart Materials and Structures* 23(9): 094001.

Robertson MA, Kara OC and Paik J (2021) Soft pneumatic actuator-driven origami-inspired modular robotic "pneumagami". *The International Journal of Robotics Research* 40(1): 72–85.

Rus D and Tolley MT (2018) Design, fabrication and control of origami robots. *Nature Reviews Materials* 3(6): 101–112.

Russo M, Sadati SMH, Dong X, et al. (2023) Continuum robots: an overview. *Advanced Intelligent Systems* 5(5): 2200367.

Santoso J and Onal CD (2021) An origami continuum robot capable of precise motion through torsionally stiff body and smooth inverse kinematics. *Soft Robotics* 8(4): 371–386.

Scimeca L, Hughes J, Maiolino P, et al. (2019) Model-free soft-structure reconstruction for proprioception using tactile arrays. *IEEE Robotics and Automation Letters* 4(3): 2479–2484.

Shen Z, Zhao Y, Zhong H, et al. (2021) Soft origami optical-sensing actuator for underwater manipulation. *Frontiers in Robotics and AI* 7: 616128.

Sivaperuman Kalairaj M, Cai CJ, Ren H, et al. (2021) Untethered origami worm robot with diverse multi-leg attachments and responsive motions under magnetic actuation. *Robotics* 10(4): 118.

Suh J-E, Miyazawa Y, Yang J, et al. (2022) Self-reconfiguring and stiffening origami tube. *Advanced Engineering Materials* 24(5): 2101202.

Suzuki H and Wood RJ (2020) Origami-inspired miniature manipulator for teleoperated microsurgery. *Nature Machine Intelligence* 2(8): 437–446.

Tachi T (2010) Geometric considerations for the design of rigid origami structures. In: *Proceedings of the International Association for Shell and Spatial Structures (IASS) Symposium*. Elsevier Ltd, Vol. 12, pp. 458–460.

Thuruthel TG, Falotico E, Renda F, et al. (2018) Model-based reinforcement learning for closed-loop dynamic control of soft robotic manipulators. *IEEE Transactions on Robotics* 35(1): 124–134.

Thuruthel TG, Shih B, Laschi C, et al. (2019) Soft robot perception using embedded soft sensors and recurrent neural networks. *Science Robotics* 4(26): eaav1488.

Toshimitsu Y, Wong KW, Buchner T, et al. (2021), Sopra: fabrication and dynamical modeling of a scalable soft continuum robotic arm with integrated proprioceptive sensing. In: 2021 IEEE/RSJ International Conference on Intelligent Robots and Systems (IROS), Prague, Czech Republic, 27 September–1 October 2021, IEEE, pp. 653–660.

Truby RL, Della Santina C and Rus D (2020) Distributed proprioception of 3D configuration in soft, sensorized robots via deep learning. *IEEE Robotics and Automation Letters* 5(2): 3299–3306.

Turner N, Goodwine B and Sen M (2016) A review of origami applications in mechanical engineering. *Proceedings of the Institution of Mechanical Engineers - Part C: Journal of Mechanical Engineering Science* 230(14): 2345–2362.

Vander Hoff E, Jeong D and Lee K (2014), Origamibot-I: a thread-actuated origami robot for manipulation and locomotion. In: Proceedings of the IEEE/RSJ International Conference on Intelligent Robots and Systems (IROS), Chicago, IL, USA, 14–18 September 2014, pp. 1421–1426.

Wang J and Chortos A (2022) Control strategies for soft robot systems. *Advanced Intelligent Systems* 4(5): 2100165.

Wang H, Totaro M and Beccai L (2018) Toward perceptive soft robots: progress and challenges. *Advanced Science* 5(9): 1800541.

Webster RJ III and Jones BA (2010) Design and kinematic modeling of constant curvature continuum robots: a review. *The International Journal of Robotics Research* 29(13): 1661–1683.

Weichart J, Roman C and Hierold C (2021) Tactile sensing with scalable capacitive sensor arrays on flexible substrates. *Journal of Microelectromechanical Systems* 30(6): 915–929.

Westra K, Dunne F, Kulsa S, et al. (2021) Compliant polymer origami bellows in cryogenics. *Cryogenics* 114: 103226.

Wirekoh J, Valle L, Pol N, et al. (2019) Sensorized flat pneumatic artificial muscles (SFPAM) embedded with biomimetic microfluidic sensors for proprioceptive feedback. *Soft Robotics* 6(6): 768–777.

Yang J, Tang D, Ao J, et al. (2020) Ultrasoft liquid metal elastomer foams with positive and negative piezo-permittivity for tactile sensing. *Advanced Functional Materials* 30(36): 2002611.

Yasuda H, Yein T, Tachi T, et al. (2013) Folding behaviour of Tachi–Miura polyhedron bellows. *Proceedings Mathematical, Physical, and Engineering Sciences* 469(2159): 20130351.

Yi J, Kim B, Cho K-J, et al. (2023) Underactuated robotic gripper with fiber-optic force sensing tendons. *IEEE Robotics and Automation Letters* 8(11): 7607–7614.

Yu M, Yang W, Yu Y, et al. (2020) A crawling soft robot driven by pneumatic foldable actuators based on miura-ori. *Actuators* 9: 26.

Zaghloul A and Bone GM (2023) Origami-inspired soft pneumatic actuators: generalization and design optimization. *Actuators* 12: 72.

Zhang Z, Wang X, Wang S, et al. (2019) Design and modeling of a parallel-pipe-crawling pneumatic soft robot. *IEEE Access* 7: 134301–134317.

Zhang Z, Chen G, Fan W, et al. (2020) A stiffness variable passive compliance device with reconfigurable elastic inner skeleton and origami shell. *Chinese Journal of Mechanical Engineering* 33: 1–13.

Zhang Q, Fang H and Xu J (2021) Yoshimura-origami based earthworm-like robot with 3-dimensional locomotion capability. *Frontiers in Robotics and AI* 8: 271.

Zhang Q, Fang H and Xu J (2023) Tunable dynamics in yoshimura origami by harnessing pneumatic pressure. *Journal of Sound and Vibration* 544: 117407.

Zhang Q, Tan K, He Z, et al. (2024) An origami continuum manipulator with modularized design and hybrid actuation: accurate kinematic modeling and experiments. *Advanced Intelligent Systems* 6(4): 2300468.

Zhou J, Chen Y, Chen X, et al. (2020) A proprioceptive bellows (PB) actuator with position feedback and force estimation. *IEEE Robotics and Automation Letters* 5(2): 1867–1874.

Zhu Y, Schenk M and Filipov ET (2022) A review on origami simulations: from kinematics, to mechanics, toward multiphysics. *Applied Mechanics Reviews* 74(3): 030801.

Zou X, Liang T, Yang M, et al. (2021) Based robotics with stackable pneumatic actuators. *Soft Robotics*.